Metal Halide Perovskite Nanostructures and Quantum Dots for Photocatalytic CO_2 Reduction: Prospects and Challenges

Huilong Liu [a], *and Shubhra Bansal* [a,b] *

[a.] *Center for Energy Research, Department of Mechanical Engineering, University of Nevada, Las Vegas, NV, USA.*
[b.] *School of Mechanical Engineering, School of Materials Engineering, Purdue University, West Lafayette, IN 47906, USA*

E-mail: bansal91@purdue.edu

Photocatalytic CO_2 reduction is a promising technology for production of solar fuels to address global environmental concerns. Metal halide perovskite (MHP) nanocrystals and quantum dots possess excellent features like high surface-to-volume ratio, broad visible-light absorption range, tunable bandgap, and high defect tolerance, making them ideal candidates for photocatalytic applications. Since the initial studies in 2017, numerous efforts have been devoted to boost the performance of MHP nanocrystals for photocatalytic CO_2 conversion. In this review, we briefly state the fundamentals, basic properties, and recent progress in the use of MHP nanocrystals for photocatalytic CO_2 reduction. Structural modifications of MHP nanocrystals are then summarized for enhanced photocatalytic performance, and they can be roughly divided into two directions: direct modulation of the pristine nanocrystals and construction of heterostructure composites. Subsequently, we lay particular emphasis on the issues obstructing MHP nanocrystals based photocatalysis from practical application, specifically, reaction systems/platforms and the toxicity of Pb. The latest groundbreaking progress including the development of novel photocatalytic system/platform and the construction of lead-free MHP nanocrystal photocatalysts are then discussed. Finally, we highlight the outlook of the MHP nanocrystals towards photocatalytic CO_2 reduction.

Key words: Metal halide perovskite, Photocatalytic catalyst, CO_2 photoreduction, nanocrystals

1. Introduction

In the past decades, the unsustainable and superfluous consumption of fossil fuels has been causing inevitable impacts like depletion of natural resources and excessive emission of carbon dioxide (CO_2) [1]. The continuously increasing CO_2 emission has been over what our atmosphere can endure, leading to the destruction of carbon circulation and finally resulting in the greenhouse effect and changes to the climate [2]. In nature, the process of photosynthesis transforms CO_2 with H_2O under sunlight to carbohydrates and O_2 at room temperature, which has been recognized as the most important pathway to maintain the relative equilibrium of CO_2 and O_2 on the earth. Inspired by the natural and efficient energy conversion exhibited by photosynthesis, the artificial photosynthesis (photocatalysis) using solar light to drive CO_2 conversion into value-added fuel is a promising pathway to mitigate environmental issues associated with green-house gas concentrations and reduce dependence on fossil fuels, simultaneously [3,4].

Since the pioneering work of Fujishima et al. [5] in 1979, which demonstrated CO_2 reduction with heterogeneous photocatalysts, extensive efforts have been devoted to developing novel photocatalysts such as metal oxides, nitrides, sulfides, selenides, chalcogenides, metal organic frameworks (MOFs) and perovskite oxides [6–15]. Although significant progress has been made, a great number of these photocatalysts still suffer from several drawbacks, such as narrow visible light harvesting resulting from the wide bandgap, rapid recombination of photogenerated charge carriers, high-cost and complex synthetic/passivation processing and poor long-term stability [4,16,17].

In the recent past, metal halide perovskites (MHPs) have emerged rapidly as the burgeoning material family with excellent optoelectronic properties such as broad visible-light absorption range, tunable bandgap, high extinction coefficient, long carrier diffusion length and lifetime, and high defect tolerance [18–20]. More

importantly, MHPs can be easily and cost-effectively synthesized as nanocrystals or quantum dot structures, which possess high surface-to-volume ratio and tunable chemical composition and structure [21–23]. The excellent photoelectric properties in conjunction with the high surface-to-volume ratio makes perovskite quantum dots (QDs) a new material platform for photocatalytic applications [16,24–29]. In 2017, Hou et al. [30] first reported the application of pure $CsPbBr_3$ QDs in photocatalytic conversion of CO_2 into CO and CH_4. Since then, numerous efforts have been made to boost the performance of halide perovskite nanocrystals and quantum dots towards photocatalytic CO_2 reduction. The improvements mainly focus on the optimization in three aspects: (1) photon absorption and charge carrier generation, (2) charge separation and migration from interior to surficial reaction sites, and (3) redox reactions mediated by the photogenerated electrons and holes at the surficial active sites.

In this review, we first briefly describe the basic mechanisms of photocatalytic CO_2 reduction, and the properties of halide perovskite nanocrystals, primarily $CsPbBr_3$. Then, we describe the recent developments in the use of MHP nanocrystals and heterostructure composites for CO_2 reduction. Subsequently, we discuss the limitations due to the reaction systems and toxicity of Pb. Finally, the promise of Pb-free halide perovskites for photocatalytic CO_2 reduction is discussed.

2. Basic Mechanisms

2.1. Mechanisms of Photocatalytic CO_2 Reduction

CO_2 is one of the most thermodynamically stable and inert compounds, possessing two double bonds with linear configuration (O=C=O angle is 180°, C=O bond length is 1.16 Å), whose bond energy (~750 kJ/mol) is higher than many other chemical bonds such as C-H (~430 kJ/mol) and C-C (~336 kJ/mol) [15]. Owing to the high activation barrier, the traditional thermal catalytic CO_2 conversion is typically a high-energy process, which requires high temperatures, pressures, and/or reactant energy [31]. Photocatalysis offers an attractive alternative for CO_2 conversion as a green process with lower operating temperatures under ambient conditions. Through the monodentate or bidentate coordinate process illustrated in **Figure 1**, the inert linear CO_2 molecules bind to the surface of photocatalysts in a bent configuration through chemisorption. In this case, the CO_2 molecules exhibit a lower lowest unoccupied molecular orbital level (LUMO), which is more susceptible to receiving electrons from the catalyst, resulting in lower activation barrier [31]. After the electron-transfer process, the surface-bound CO_2^-

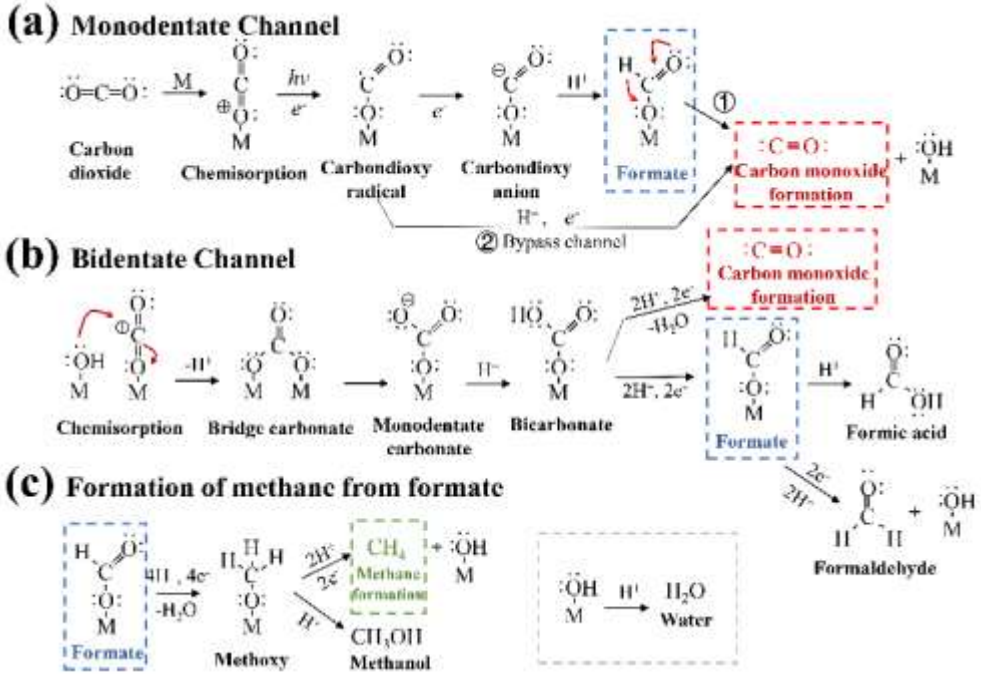

Figure 1. Photocatalytic reaction mechanisms of CO_2 reduction, with two possible pathways.

with more reactive nature is formed, which facilitates further reaction producing a series of hydrocarbons through two different pathways [32].

The photocatalytic CO_2 conversion is generally performed in a closed gas-circulating cell, where the CO_2 (dissolved in solvents or mixed with water vapor) gets reduced in the presence of semiconductor as photocatalyst under illumination. Correspondingly, two typical reaction systems namely the "solid-liquid system" and "solid-vapor system" are illustrated in **Figure 2a**. In the solid-liquid system, the photocatalyst particles are dispersed in the solvent where CO_2 is dissolved, while the CO_2 is typically blended with the electron-donating vapor (e.g., water) in solid-vapor system. For all reaction systems, photocatalysis has three broad steps, namely photoexcitation, charge separation/transfer, and surface chemical reactions, as illustrated in **Figure 2b**. In the first step (α), photocatalysts absorb photons with energy greater than/equal to their bandgap (E_g) to generate charge carriers. The photogenerated charge carriers can follow different routes: trapped at a defect site (β_1); radiative or non-radiative recombination (β_2); and/or diffusion to the reaction site (β_3). As the carrier recombination rate is much faster (10^{-9} s) compared to photocatalytic reaction rates (γ) (~10^{-3}–10^{-8} s) [15], many strategies for improving charge separation have been pursued, e.g., heterojunctions. Finally, in the third step (γ), the electrons and holes reaching the surface are transferred to the adsorbed reactant species (e.g., CO_2 and H_2O) and partake in the reduction and oxidation reactions, respectively. In addition, the band edge positions are important to favorably drive the redox reactions. In the CO_2 reduction reaction using water as hole scavenger, for example, conduction band minimum (CBM) of the photocatalysts should be more negative than the reduction potential of CO_2 (-0.52 V vs. RHE for CO_2 to CO at pH 7) to allow photogenerated electrons to effectively transfer to CO_2. At the same time, the valence band maximum (VBM) of the photocatalysts should be more positive than the oxidation potential of H_2O to form O_2 (0.81 V vs. RHE at pH 7) with ready access to photogenerated holes.

The band-edge positions of typical photocatalysts and MHPs relative to the reversible hydrogen electrode (RHE) at pH 7 and the redox potential of some common half-reactions are shown in **Figure 2c**. Since CO_2 photoreduction is a rather complex reaction that involves multiple electrons, various products via different reaction pathways (as shown in **Figure 1**) can form. The selectivity of product formation during CO_2 reduction remains complicated and depends on numerous factors, such as CO_2 adsorption mode, pH of the solution, functional groups, and co-catalysts, etc. Especially, the adsorption/desorption of products or intermediates on photocatalysis plays a significant role in determining selectivity. The weakly bonded intermediates may desorb before being converted to the final products. Conversely, the final products should not bind strongly to avoid further conversion or reverse reaction.

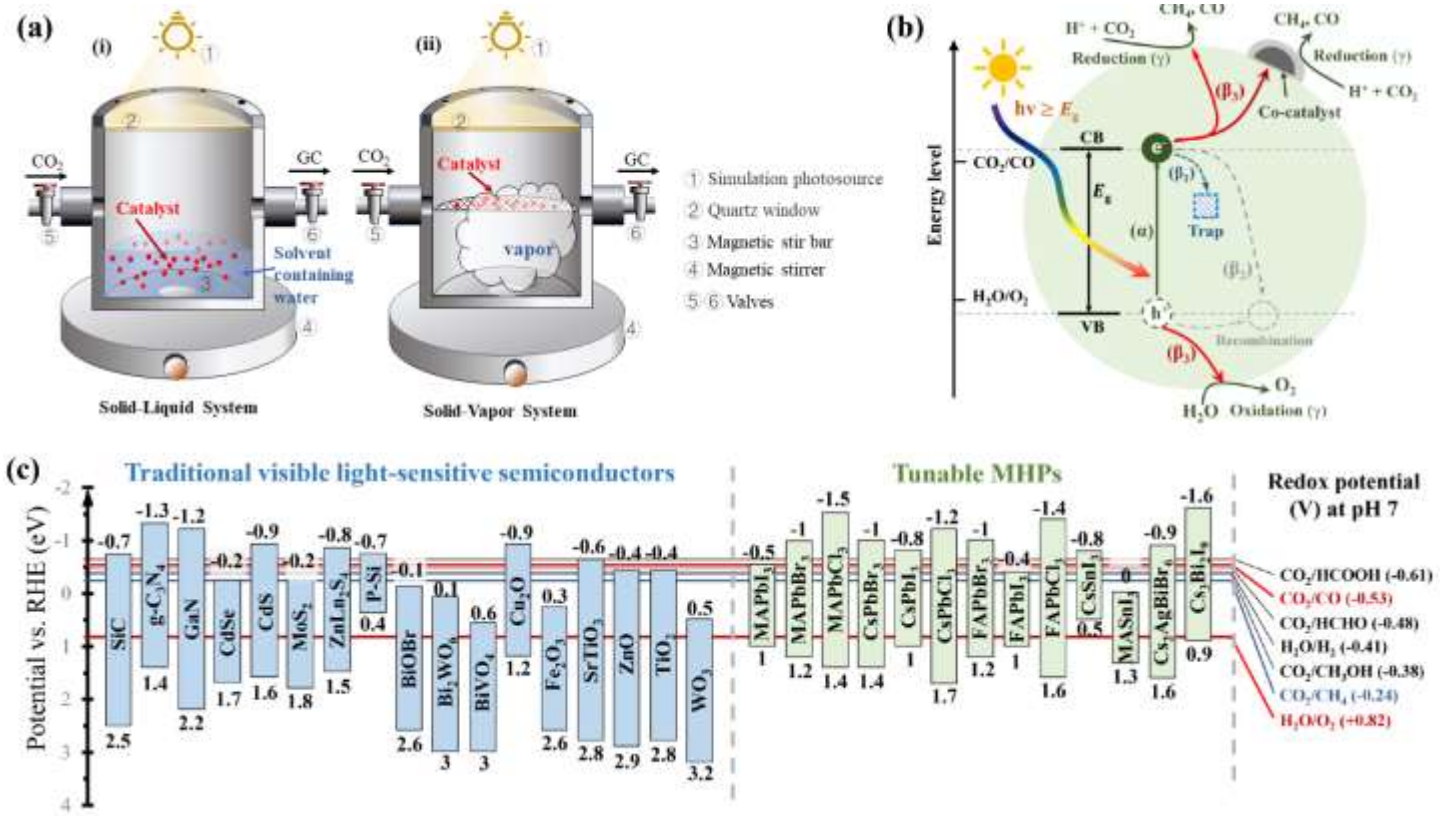

Figure 2. (a) Two typical reaction systems for photocatalytic CO_2 reduction: (i) Solid-liquid system and (ii) Solid-vapor system. (b) Schematic illustration of the three-step process of photocatalytic CO_2 reduction in presence of H_2O. (c) Band edge position of conventional photocatalysts and different MHPs relative to reversible hydrogen electrode (RHE). For comparison, the redox potentials of some significant half-cell reactions are also shown.

2.2. Mechanisms of CO_2 Reduction with Halide Perovskites

Metal halide perovskites ABX_3 contain eight corner-sharing octahedra BX_6^- with metal cation (B=Pb, Bi, or Sn) in the center, forming the perovskites' ideal cubic structure as shown in **Figure 3a**. Here, A cation is methylammonium (MA), formamidinium (FA), or Cs at the cuboctahedra cavity and vertices of the octahedra are halide anions (X=Cl, Br, or I). Halide perovskites have already shown great promise in a wide range of technological applications including photovoltaics (PV), light-emitting diodes (LEDs), lasers, transistors, and photodetectors [21,22]. These successes have motivated the use of MHPs as photocatalysts over conventional semiconductors [25]. Metal halide perovskites offer a vast and potentially attractive window for photocatalytic CO_2 reduction, owing to their tunable bandgap and band-edges as shown in **Figure 2c** [31]. The most explored composition for photocatalytic applications is $CsPbX_3$, the band structure for which is shown in **Figures 3c-d**. In $CsPbX_3$, the valence band is dominated by the halide p orbitals with only minor contributions from Pb 6s orbitals, and the conduction band is formed by the overlap of Pb 6p-orbitals. Therefore, VBM is sensitive to the choice of halide ions and the increase in bandgap with substitution of I- to Br- to Cl is predominately driven by the downward shift of valence band [33–35].

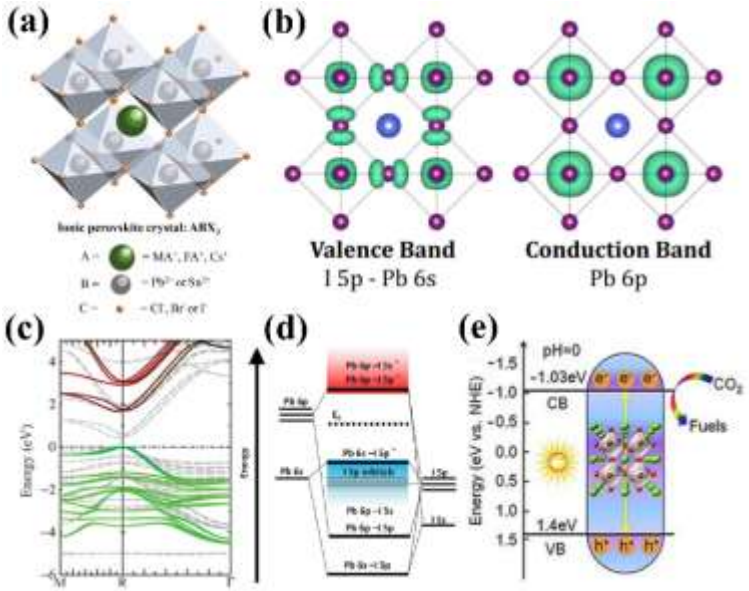

Figure 3. (a) Ideal cubic structure of conventional MHPs ABX_3. (b) Electron density calculation corresponding to the valence band maximum and conduction band minimum of cubic $CsPbI_3$. Reprinted with permission from Ref. 33. Copyright 2015, American Chemical Society. (c) Band structure of $MAPbI_3$ perovskites. Reprinted with permission from Ref. 34. Copyright 2014, American Physical Society. (d) Energy band diagram of the $MAPbI_3$ perovskites. Reprinted with permission from Ref. 35. Copyright 2003, American Physical Society. (e)Schematic illustration of mechanism of photocatalytic CO_2 reduction. Reprinted with permission from Ref. 30. Copyright 2017, Wiley-VCH.

Early research on halide perovskite nanocrystals for photocatalytic CO_2 reduction was conducted by Hou et al. in 2017 [30], wherein, $CsPbBr_3$ nanocrystals with tunable size (3-12 nm) were synthesized using the "hot-injection method". Superior to single crystals or microcrystals, MHP quantum dots and nanocrystals offer following merits: (1) ability to tune the bandgap and band-edge potentials with quantum confinement size regime (2) decrease in density of bulk recombination defects (3) better CO_2 absorption at photocatalyst due to higher surface-to-volume ratio, and (4) higher drift/diffusion rates of photogenerated electrons to reaction sites. The 8.5 nm $CsPbBr_3$ nanocrystals obtained at 170℃ showed a bandgap of 2.43 eV and high absorption coefficient (**Figure 3e**). Meanwhile, their suitable band potential (CBM~ -1.03 eV and VBM~ 1.4 eV, vs. NHE at pH 0) endowed the photogenerated electrons-holes pairs with enough drive force for CO_2 reduction [$E^\circ(CO_2/CO)$ = -0.52 V and $E^\circ(CO_2/CH_4)$ = -0.24 V, vs. NHE] accompanied with water oxidization [$E^\circ(O_2/H_2O)$ = 0.82 V vs. NHE]. $CsPbBr_3$ nanocrystals exhibited photocatalytic activity towards CO_2 reduction in ethyl acetate/ water reaction medium, reaching an average electron yield rate ($R_{electron}=2R_{CO}+8R_{CH4}+2R_{H2}$) of 20.9 μmol $g^{-1}h^{-1}$. The key limitations identified for $CsPbBr_3$ nanocrystals include insufficient charge carrier separation, material instability, and the lack of intrinsic surface catalytic sites due to the inferior surface activity of lead ions and its poor distribution on the MHP nanocrystal surface. Significant efforts have been made to improve light harvesting, charge separation, and reaction activity in MHP nanocrystals including intrinsic improvements as well as heterojunction creation summarized in the following sections.

3. Device Architecture

3.1. Intrinsic Improvements to Halide Perovskites

3.1.1. Morphology and Dimensionality

The change in morphology and dimensionality of MHP nanocrystals can make a critical difference in their photocatalytic activity for CO_2 reduction. In the study of Hou et al. [30], for example, the $CsPbBr_3$ NCs of various sizes (3.8 nm, 6.1 nm, 8.5 nm, and 11.6 nm) were observed with diverse performance towards solar-driven CO_2 reduction. The variances mainly derived from the intrinsic quantum size effects which effectively regulated the bandgap (**Figure 4b**) and optical absorption of $CsPbBr_3$ NCs over the visible spectral region (**Figure 4a**). Besides, particle size also affected the aggregation, surface area/sites, and charge diffusion path of $CsPbBr_3$ NCs, leading to differences in catalytic activities (**Figure 4c**). In a word, modulation and optimization of the $CsPbBr_3$ particle size played an essential role determining its performance towards solar-driven CO_2 reduction. Recently, Wu and his colleagues [36] successfully synthesized the 2D MHP nanosheets of various thicknesses (2, 3, 4, and 4.6 nm) and firstly applied them as photocatalysts for the reduction of CO_2, with H_2O acting as electron donor. Compared with $CsPbBr_3$ NCs, the nanosheets presented significantly higher activity and improved stability for photocatalytic CO_2 reduction stemming from following unique features: (1) 2D structure led to better stability in water-containing systems; (2) large proportion of low-coordinated metal atoms exposed more active sites for CO_2 reduction; (3) The shortened carrier diffusion distance from internal to surface decreased bulk recombination. In addition, the quantum confinement effect caused by vertical dimension decrease was also observed in the $CsPbBr_3$ nanosheets. As the thickness decreased from 4.6 to 2 nm, the first absorption peak of $CsPbBr_3$ nanosheets shifted from 454 to 429 nm (**Figure 4d**), associated with higher direct bandgap (**Figure 4e**). The thickness of $CsPbBr_3$ nanosheets had significant impacts on photocatalytic CO_2 reduction to CO, with 4 nm-thick sheets showing the highest activity. The CO generation rate reached 21.6 μmol $g^{-1}h^{-1}$, which was 3.8 times higher than that of $CsPbBr_3$ NCs (5.7 μmol $g^{-1}h^{-1}$). The 4 nm $CsPbBr_3$ nanosheets showed an optimal combination of photon absorption, active reaction sites and carrier transport for CO_2 reduction in presence of H_2O. Moreover, Shyamal et al. [37] offered an insightful perspective on morphological effect of MHP nanocrystals for CO_2 reduction. In this study, $CsPbBr_3$ nanocrystals in conventional six-faceted cube (**Figure 4i**) and unique faceted noncubic shapes (polyhedron-shape (**Figure 4g**) and six-armed hexapods shape (**Figure 4h**)) were prepared and explored for photocatalytic CO_2 reductions in a standard ethyl acetate/water medium, respectively. As shown in **Figure 4f**, the conventional cubic $CsPbBr_3$ showed poor catalytic activity towards CO_2 reduction (generation yield of 16.4 μmol g^{-1} for CO, and 7.6 μmol g^{-1} for CH_4), while the halide-deficient noncubic orthorhombic-phase $CsPbBr_3$ with new facets was observed as a superior catalyst (generation yield of 130 μmol g^{-1} for CO and 58.8 μmol g^{-1} for CH_4). Besides, the complex hexapod structured $CsPbBr_3$ nanocrystals also exhibited intermediate catalytic performance (generation yield of 79.5 μmol g^{-1} for CO and 38.4 μmol g^{-1} for CH_4). The enhancement in the photocatalytic activities of the dimensionally modified $CsPbBr_3$ nanocrystals was ascribed to the suppressed charge recombination and the new active exposed facets. A large number of surface defects existed on the noncubic shaped $CsPbBr_3$ nanocrystals due to halide vacancies, forming Pb-rich reaction sites. Additionally, these surface trap states facilitate transfer of photogenerated electrons to the reaction sites to trigger chemical reactions shown in **Figure 4j**. It inhibited fast carrier recombination process and provided an opportunity for efficient charge transfer in triggering catalytic reactions. Besides, compared to the dominant {002} and {110} facets of traditional orthorhombic cubic shaped $CsPbBr_3$ nanostructures, the new exposed {112} and {102} facets exhibited more adaptable surface adsorption/desorption energies of CO_2 and the reduction products, which also supported more efficient catalytic performance in converting light to chemical energy.

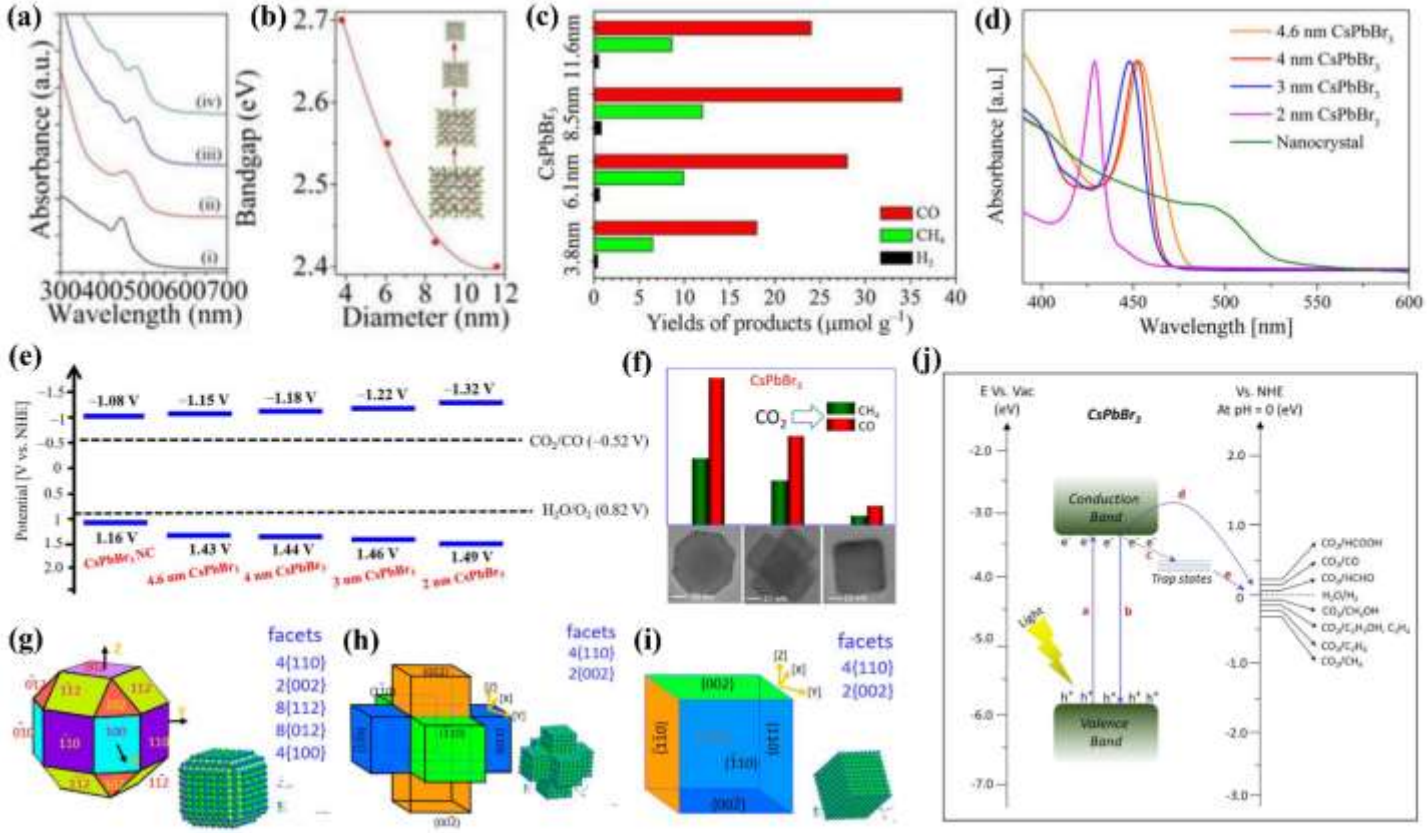

Figure 4. Morphology and dimensionality modulation of the pristine MHP nanocrystals. (a) The UV/Vis absorption spectra and (b) the bandgap of $CsPbBr_3$ QDs with different particle sizes: (i) 3.8, (ii) 6.1, (iii) 8.5, and (iv) 11.6 nm. (c) The CO_2 reduction performance of $CsPbBr_3$ QDs with different particle sizes. Figures (a), (b), and (c) are reprinted with permission of Ref.30. Copyright 2017, Wiley-VCH. (d) The UV-Vis absorption spectra of $CsPbBr_3$ nanocrystal and $CsPbBr_3$ nanosheets with different thicknesses. (e) Band structures of $CsPbBr_3$ nanocrystals and nanosheets. Figures (d) and (e) are reprinted with permission of Ref. 36. Copyright 2021, Wiley-VCH. (f) CO_2 reduction performance of $CsPbBr_3$ nanostructure with different shapes: polyhedrons, hexapods, and cubic, respectively. The structural models of (g) polyhedron-shaped, (h) hexapods, and (i) cube-shaped $CsPbBr_3$ nanostructures, respectively. (j) Band structure of $CsPbBr_3$ photocatalysts with relative potential of CO_2 reduction. Figures (f)-(j) are reprinted with permission of Ref. 37. Copyright 2020, American Chemical Society.

3.1.2. Surface Modulation

The surface characteristics of MHP nanocrystals play an essential role in regulating the photocatalytic process of CO_2 adsorption, activation, and conversion. The pristine $CsPbBr_3$ nanocrystals synthesized through conventional methods resulted in halogen-rich surface (**Figure 5a**) [38], which effectively passivated surface traps and improved the photoluminescence quantum yield (PLQY), suitable for application in lighting and displays. However, the typical halogen-rich surface has shown to be detrimental for photocatalytic applications as the Pb^{2+} active sites are isolated interiorly. The conduction band minimum (CBM) of $CsPbBr_3$ nanocrystals mainly stemmed from 6p orbitals of Pb, while the valance band maximum (VBM) was predominantly contributed by Br 4p orbitals (**Figure 5b**) [39]. Pristine $CsPbBr_3$ nanocrystals have a relatively inert halide-rich surface, which inhibits the diffusion of photogenerated electrons from conduction band to the surface for subsequent reduction reactions. Zhu et al. [40] have reported synthesis of $CsPbCl_3$ nanocrystals via a liquid-solid interpenetration (LSI) method (**Figure 5 c**) covered with a dense Pb-rich protective structure. The Pb-rich layers act as water-blocking barriers resulting in high stability, enable mono-dispersity, and expose large number of active sites for

photoreduction reactions. Consequently, under simulated solar irradiation, Pb-rich Ni-doped $CsPbCl_3$ nanocrystals presented an outstandingly boosted rate towards CO_2 photoreduction (generation rate of 169.37 μmol $g^{-1}h^{-1}$ for CO) compared to that of Ni-doped $CsPbCl_3$ nanocrystals without an LSI treatment (generation rate of 8.55 μmol $g^{-1}h^{-1}$ for CO) (**Figure 5d**). The Ni-doping here was also for the promotion of photocatalytic performance, which is to be discussed in later section.

In addition, effects of ligand density on the MHP nanocrystals should also be considered. The pristine MHP nanocrystals are usually capped by long aliphatic chain-containing organic ligands such as oleic acid (OA) and oleylamine (OAm). It was demonstrated that ligands had a dual effect on MHP nanocrystals: on one hand, an appropriate density of surface organic ligands prevented the agglomeration of the nanocrystals and provided sufficient passivation of surface dangling bonds. On the contrary, excessive insulating organic ligands: (1) hampered the diffusion of photogenerated carriers from photocatalysts to reactants, (2) inhibited absorption of potential substrate (e.g., CO_2) on active sites, and/or (3) accumulated the photoconversion products and intermediates to cause catalyst poisoning, all detrimental to photocatalytic activity of the MHP nanocrystals. Therefore, optimal surface ligand density is crucial for high performance and good stability. In fact, the conventional surface ligands (OA and OAm) on MHP nanocrystals exhibit a highly dynamic binding state due to the strong electronegativity of nitrogen atoms and reversible protonation/deprotonation process. For example, pristine $CsPbBr_3$ nanocrystals are typically terminated with Br^- and the OAm^+ ions interact with Br^- through hydrogen bonds as capping ligands by substituting Cs^+ ions from the surface (**Figure 5e**) [41]. The formation of hydrogen bonds reduces the coulombic interactions between Pb^{2+} and Br^- ions, thus in the presence of certain solvent molecules (e.g., ethyl acetate), the ammonium ligands may fall off from the nanocrystal surface along with Br^- ions (**Figure 5f**) [39]. Accordingly, partial capping ligands can be stripped and leaving Pb^{2+}/Cs^+ metal sites (and surface trap state) on the $CsPbBr_3$ nanocrystal surface (**Figure 5g and 5h**) [39,42], which renders a valid tactic optimizing ligand density of the MHP nanocrystals. For instance, in the study of Zhou et al. [43], the as-prepared $Cs_2AgBiBr_6$ nanocrystals were washed by absolute ethanol to avoid the negative influence of the ligands prior to the photocatalytic CO_2 reduction reactions. The wash process effectively decreased the ligand density while retaining the crystal structural integrity and stability of the $Cs_2AgBiBr_6$ nanocrystal. As the results shown in **Figure 5i**, $Cs_2AgNiBr_6$ NCs subjected to wash process exhibited boosted conversion rate of CO and CH_4, respectively, presenting a 6.5-fold enhancement in electron consumption rate ($R_{electron}$) compared to unwashed nanocrystals. The enhancement was attributed to the more efficient transfer of carriers and products, due to decreased ligand density after the washing with absolute ethanol. Optimization of purification process was also verified as a practical strategy to control ligand density on the as-synthesized MHP nanocrystals. Of the conventional purification solvents, ethyl acetate (EA), a non-polar solvent, is appropriate for the purification of ionic MHP nanocrystals. Chen et al. [44] regulated the ligand density on the surface of $CsAgInCl_6$ nanocrystals via changing volume ratio of hexane/EA (1:1, 1:2, 1:3, and 1:4) in the purification process, corresponding to processes I-IV, respectively. The ligand content decreased gradually through the purification of various processes. Specifically, the composites that underwent purification process I showed large resistance to charge transfer, due to high surface ligands density. Agglomeration of the composites occurred after processes III and IV since most of the ligands had fallen off after an intensive purification, and the resultant large surface energy drove agglomeration of the over-exposed composite nanocrystals. Outstandingly, the "CAIC QDs@Ag-2" composite purified with process II exhibited optimal separation efficiency of the charge carriers. All these results not only confirmed the purification process control as effective strategy to optimize the ligand density, but also emphasized the significance of appropriate surface ligand density for charge transport in MHP nanocrystals. With the application of ethyl acetate, Chen et al. [45] replaced the native insulating long-chain organic ligands (OA and OAm) on pristine $CsPbBr_3$ with small PF_6^- ligands, which offered a nearly pristine surface with low charge-transfer resistance. As illustrated in **Figure 5j**, EA treatment spited the bonds between $CsPbBr_3$ NCs and the native organic ligands, resulting in a more positive surface due to the Pb^{2+}/Cs^+ metal sites (halogen vacancies) (**Figure 5k**). The positively charged surface then facilitated the immobilization of a higher amount of PF_6^- on the $CsPbBr_3$ NCs via electrostatic interactions. After ligand substitution, the PF_6^--$CsPbBr_3$ exhibited a higher CO/CH_4 generation rate from CO_2 reduction compared to the pristine $CsPbBr_3$ that showed very limited catalytic activity (**Figure 5l**). The enhancement was attributed to the low surface charge transfer resistance upon stripping the

native ligands, which facilitated the transfer of photogenerated electrons to nanocrystal surface for redox reactions. Besides, the shedding of these bulky capping ligands also eliminated the barrier hindering further assembly of cocatalysts ($CsPbBr_3$-Ni(tpy)) and charge transfer from $CsPbBr_3$ NCs to cocatalysts. Here, the coupling of cocatalysts with pristine MHP nanocrystals is also a feasible method to improve the photocatalytic performance.

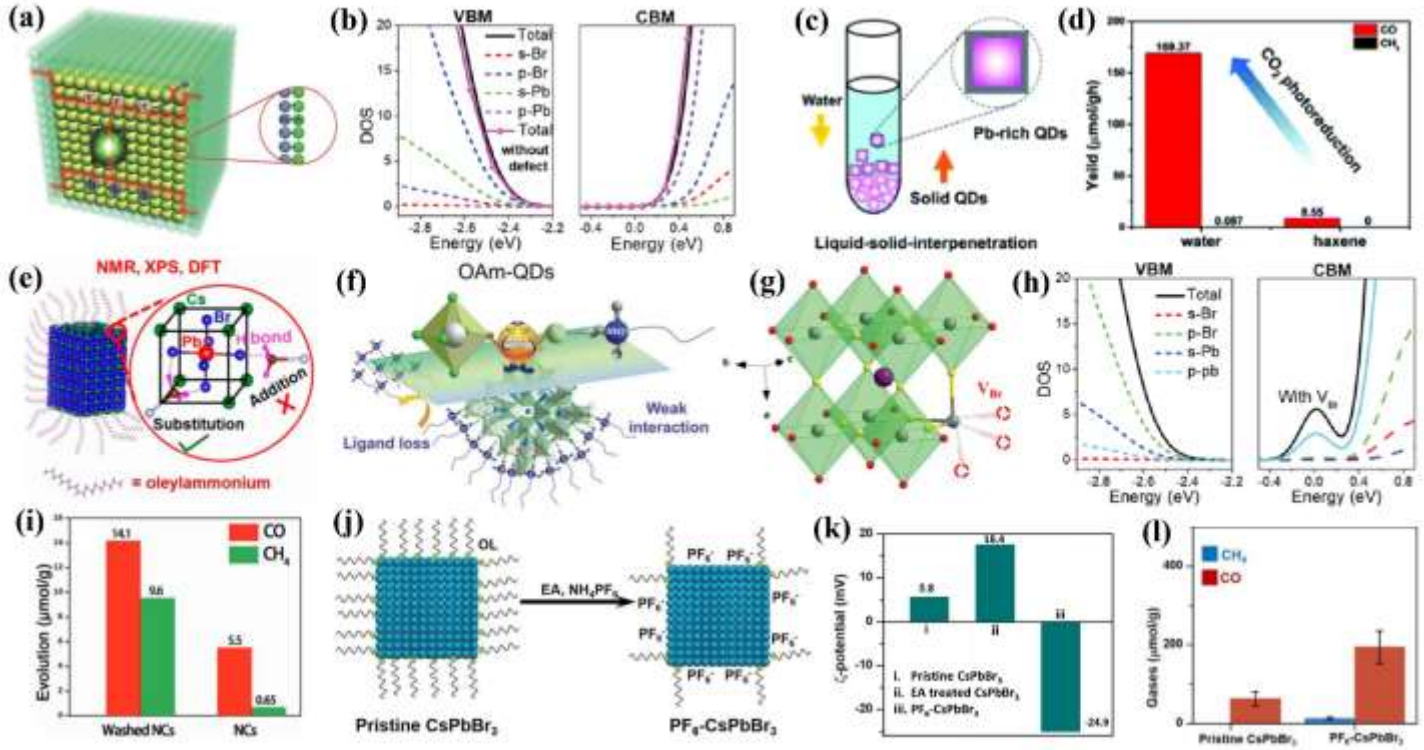

Figure 5. Surface modulation of the pristine MHPs nanocrystals. (a) Halide-rich surface of $CsPbBr_3$ nanocrystals. Reprinted with permission of Ref. 38 Copyright 2016, Wiley-VCH. (b) Electronic DOS curves of valence band maximum (VBM) and conduction band minimum (CBM) of $CsPbBr_3$ nanocrystals. (c) The liquid-solid-interpenetration (LSI) synthesis method for water-stable monodisperse Pb-rich $CsPbCl_3$ QDs. (d) Photocatalytic CO_2 reduction performances of the surface Pb-rich Ni-doped $CsPbCl_3$ QDs. Figures (c) and (d) are reprinted with permission of Ref. 40. Copyright 2020, Royal Society of Chemistry. (e) Binding of OLA^+ to $CsPbBr_3$ via hydrogen bonds. Reprinted with permission of Ref. 41. Copyright 2017, American Chemical Society. (f) The OAm ligands may fall off from the nanocrystal surface along with Br- ions in the presence of certain solvent molecules. (g) $CsPbBr_3$ QDs with V_{Br} surface defect types. Reprinted with permission of Ref. 42. Copyright 2016, Wiley-VCH. (h) Electronic DOS curves of VBM and CBM of $CsPbBr_3$ with V_{Br}. Figure (b), (f), and (h) are reprinted with permission of Ref.39. Copyright 2019, Wiley-VCH. (i) The CO_2 reduction performance of the as-prepared $Cs_2AgBiBr_6$ NCs and absolute ethanol washed NCs, respectively. Reprinted with permission of Ref. 43. Copyright 2018, Wiley-VCH. (j) Schematic of the substitution of OL with PF_6^-. (k) Variations in the zeta (ζ) potentials of the pristine $CsPbBr_3$ through the substitution process of OL with PF_6^-. (l) Photocatalytic CO_2 reduction performance of pristine $CsPbBr_3$ and PF_6-$CsPbBr_3$, respectively. Figures (j)-(l) are reprinted with permission of Ref. 45. Copyright 2020, American Chemical Society.

3.1.3. Composition Engineering

In addition to changes in morphology, dimensionality, and surface modulation; composition engineering is another lever to effectively boost the photocatalytic performance of MHP nanocrystals and quantum dots. Specifically, changes in composition can include ionic intermixing and doping of metal ions.

3.1.3.1. Halide Substitution

Halide substitution can tune the bandgap and band edge positions in MHP nanocrystals, thereby controlling photon absorption, number of photogenerated carriers and the driving force for photocatalytic redox reaction. Cheng et al. [46] adopted the post-synthesis anion exchange method to tune the halide ratio of $CsPbBr_3$ quantum dots (QDs) by adding ZnI_2/oleylamine/toluene solution. After anion-exchange, the color of $CsPbI_{3-x}Br_x$ QDs solution changed gradually from green to red (**Figure 6a**), accompanied by a shift in photon absorption edge from ~520 nm to ~620 nm (**Figure 6b**) and bandgap reduction from 2.4 to 1.9 eV (**Figure 6c**). In solid-vapor photocatalytic CO_2 reduction reaction with polyether sulfone (PES) as scaffold, the red I-rich $CsPbI_{2.6}Br_{0.39}$ QDs achieved an improved productivity (32.45 μmol $g^{-1}h^{-1}$ for CO with electron consumption rate of 64.90 μmol $g^{-1}h^{-1}$) compared to that of the green $CsPbBr_3$ QDs (27.22 μmol $g^{-1}h^{-1}$ for CO with electron consumption rate of 54.44 μmol $g^{-1}h^{-1}$). The promotion was mainly attributed to the narrower bandgap of $CsPbI_{2.6}Br_{0.39}$ QDs, which extended the absorption range for visible light and increased the amount of photogenerated electrons. Moreover, it was also suggested that the anion exchange may increase trap-state density, thus the overall photocatalytic performance of the QDs was in fact determined by a synergistic effect between light absorption and trap-induced recombination. Similarly, Wu et al. [36] adopt the anion exchange method to improve the narrow visible light response of the $CsPbBr_3$ nanosheets by replacing part of the Br^- with I^-. With increase in I content, the resultant $CsPbBr_{2.7}I_{0.3}$, $CsPbBr_{2.4}I_{0.6}$, and $CsPbBr_{2.1}I_{0.9}$ nanosheets exhibit redshifted absorption peaks from 452 nm to 466 nm (**Figure 6d**) and narrower direct bandgaps (2.61, 2.57, and 2.55 eV, respectively) (**Figure 6e**). Consequently, all the $CsPbBr_{3-x}I_x$ nanosheets exhibited improved activity toward photocatalytic CO_2 reduction compared to pristine $CsPbBr_3$, due to enhanced visible light-harvesting capacity via anion exchange. $CsPbBr_{2.4}I_{0.6}$ nanosheet achieved the highest CO generation rate of 43.9 μmol $g^{-1}h^{-1}$, which was over twice that of $CsPbBr_3$ nanosheets (21.6 μmol $g^{-1}h^{-1}$) (**Figure 6f**). Meanwhile, the lower photocatalytic activity of the $CsPbBr_{2.7}I_{0.3}$ and $CsPbBr_{2.2}I_{0.8}$ was attributed to the weak light harvesting and reduced thermodynamic driving force for photocatalytic CO_2 reduction, respectively. Additionally, it was also emphasized that the anion-exchange reactions increased the surface traps on the $CsPbBr_{3-x}I_x$ nanosheets, which suppressed the recombination of photogenerated carriers thereby promoting their separation and transfer efficiency, benefiting the CO_2 reduction reaction.

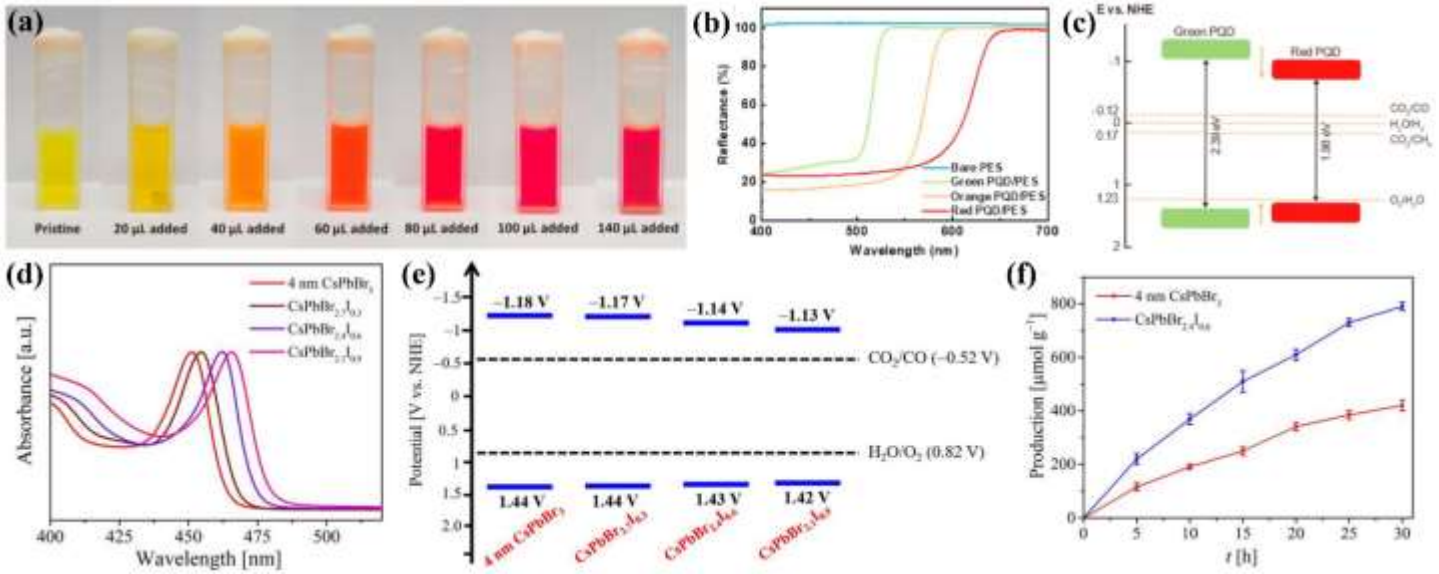

Figure 6. Halide composition tuning of the pristine MHPs nanocrystals. (a) Color changes of $CsPbBr_{3-x}I_x$ QDs solution with addition of ZnI_2 solution for anions exchange. (b) Reflection curves of bare PES membrane and PQD/PES monolithic films. (c) Band diagram of green and red QDs and energy level diagram of CO_2 photoreduction. The (a)-(c) are reprinted with permission of Ref. 46. Copyright 2021, Elsevier. (d) The UV-Vis absorption spectra of $CsPbBr_{3-x}I_x$ nanosheets with different contents of halides (Br^- and I^-). (e) The band structures of $CsPbBr_{3-x}I_x$ nanosheets with relative potential of CO_2 reduction. (f) Photocatalytic CO_2 reduction performance

(CO production rate) of 4 nm $CsPbBr_3$ nanosheets and $CsPbBr_{2.4}I_{0.6}$ nanosheets, respectively. The (d)-(f) are reprinted with permission of Ref. 36. Copyright 2021, Wiley-VCH.

3.1.3.2. Doping of Metal Ions

The doping of active metal cations on the surface of photocatalyst is also regarded as a feasible strategy for improving the photocatalytic CO_2 conversion efficiency, by increasing the active sites and enhancing the charge separation. Recently, Tang et al. [47] theoretically predicted that when Co and Fe atoms were doped into the perovskites, their catalytic capability towards CO_2 reduction would be significantly strengthened. The critical evidences presented were: (1) The adsorption of CO_2*, C*OOH and HCOO* intermediates in the Co- and Fe-doped cases was much stronger than that for the pristine case, which facilitated the CO_2* reduction and subsequent processes; (2) As shown in **Figure 7a**, the changes of free energy barriers for the formation of the intermediate molecules (ΔG) on Co- and Fe-doped cases were lower than those on the pristine case; (3) Co- and Fe-doped sites tend to capture photogenerated electrons in halide perovskite, meanwhile they hold stronger electron-donating capability than Pb in the pristine perovskite. Based on these observations, it is clear that the catalytic efficiency of the perovskite was greatly improved with Co and Fe doping. Inspired by this report, Dong et al. [48] doped cobalt (Co) on a halide perovskite nanocomposite composed of $CsPbBr_3$ embedded in a Cs_4PbBr_6 matrix (PNC) to boost its photocatalytic activity towards CO_2 reduction in a CO_2-saturated acetonitrile/water/ methanol reaction system. The Co-doped "Co1%@PNC" achieved a much higher yield of photocatalytic CO_2 reduction to CO (1835 μmol g^{-1}) compared to that of undoped PNC (678 μmol g^{-1}) in 15 h reaction. The improvement in the photocatalytic performance was attributed to the increased active sites and the improved efficiencies of photogenerated carrier transfer and separation rooting from cobalt ions serving as surface trap states (**Figure 7b**). Besides, Shyamal et al. [49] synthesized the Fe (II)-doped $CsPbBr_3$ nanocrystals via partially replacing Pb with Fe (II) and explored them for photocatalytic reduction of CO_2 in an ethyl acetate/water medium (**Figure 7c**). The 3% Fe (II) doped $CsPbBr_3$ exhibited enhanced catalytic performance (electron consumption rate of 55.2 μmol $g^{-1}h^{-1}$) for CO_2 reduction than pristine undoped $CsPbBr_3$ (24.4 μmol $g^{-1}h^{-1}$). Moreover, the doped $CsPbBr_3$ showed selectively CH_4 as the dominant product while the undoped $CsPbBr_3$ lead to CO as the major products, which was attributed to the diverse adsorption and desorption abilities of CH_4 and CO on these different catalyst surfaces. In addition, the study by Liu et al. [50] demonstrated that Mn^{2+} substitution to MHP nanocrystals could also significantly improve the photocatalytic performance. The Mn-doped $CsPbBr_xCl_{3-x}$ mixed-halide perovskites exhibited more than 14 times improvement in catalytic performance (generation yield of 1917 μmol g^{-1} for CO and 82 μmol g^{-1} for CH_4) than pristine catalysts in the 9 h reaction.

Although implantation of metal ions such as Fe, Co, Mn, et al. in MHP nanocrystals have been practically employed to improve the performance of photocatalytic CO_2 reduction, most of these studies employ in-situ doping techniques. In-situ doping can result in the bulk doping (rather than surface doping), which inversely expedited the carrier recombination and limited the enhancement of photocatalytic performance. Directly implanting active metal ions on the surface of MHP nanocrystals via post-synthetic cation-exchange was given as a possible solution to the puzzle [51], nonetheless, direct cation-exchange was hard to achieve owing to the rigid octahedron structure of $[PbX_6]$ [52]. To overcome this obstacle, Cheng et al. [53] provided a solution for the efficient post-synthetic cation-exchange of MHP nanocrystals by constructing $CsPbBr_3$ nanocrystals with partial acetate (Ac-) instead of bromide coordination. As shown in **Figure 7d**, since the bidentate Pb (II)-Ac bond was thermodynamically unfavorable, the corresponding octahedron structure containing acetate in $CsPbBr_{3-x}Ac_x$ ($[PbBr_{6-x}Ac_x]^{4-}$) should be easily opened to realize efficient surface cation-exchange of Pb^{2+} with Ni^{2+} ions. The photocatalytic CO_2 reduction reaction for Ni: $CsPbBr_{2.77}Ac_{0.23}$ under visible light exhibited significantly increased CO yield of 44.09 μmol $g^{-1}h^{-1}$, which is over 8 and 3 times higher than those of pristine $CsPbBr_3$ (5.03 μmol $g^{-1}h^{-1}$) and direct cation-exchange (Ni: $CsPbBr_3$) (14.49 μmol $g^{-1}h^{-1}$) respectively, as shown in **Figure 7e**. The enhanced photocatalytic activities of both Ni: $CsPbBr_3$ and Ni: $CsPbBr_{2.77}Ac_{0.23}$ were attributed to the higher number of active sites and substantially improved charge separation which accelerated the electron transfer from bulk to surface Ni^{2+} ions, while the higher Ni^{2+} doping rooted from the acetate assisted cation-exchange strategy interpreted the better performance on Ni: $CsPbBr_{2.77}Ac_{0.23}$.

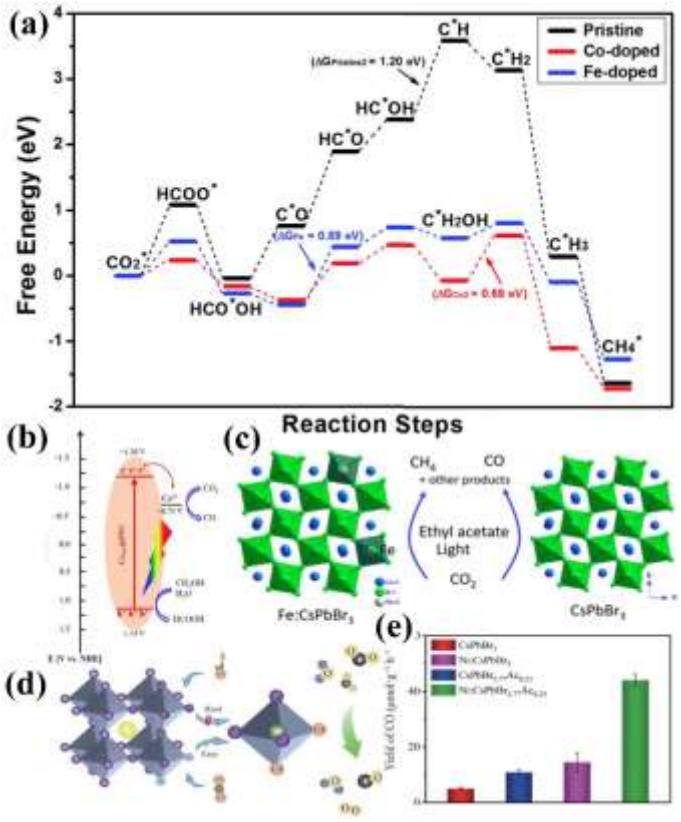

Figure 7. Doping of metal ions. (a) The free energy diagrams of the most favored paths of CO_2 reduction on pristine $CsPbBr_3$, Co-doped $CsPbBr_3$ and Fe-doped $CsPbBr_3$, respectively. Reprinted with permission of Ref. 47. Copyright 2019, Royal Society of Chemistry. (b) Band structures for Co1%@PNC and schematic illustration of the CO_2 reduction. Reprinted with permission of Ref. 48. Copyright 2020, Royal Society of Chemistry. (c) The photocatalytic CO_2 reduction reaction on Fe-doped $CsPbBr_3$ and undoped $CsPbBr_3$ nanocrystal photocatalysts with different main products. Reprinted with permission of Ref. 49. Copyright 2019, American Chemical Society. (d) Acetate-assistant cation-exchanges in cubic $CsPbBr_{3-x}Ac_x$ NCs with Ni-$(OA)_2$. (e) The CO_2 photocatalytic reduction performance (CO production rate) of the $CsPbBr_3$, Ni: $CsPbBr_3$, $CsPbBr_{2.77}Ac_{0.23}$, and Ni: $CsPbBr_{2.77}Ac_{0.23}$, respectively. The (d) and (e) are reprinted with permission of Ref. 53. Copyright 2021, Tsinghua University Press and Springer.

3.2. Heterojunction Devices

In addition to the direct modulation, integrating these pristine MHP nanocrystals with other appropriate functional materials to construct heterojunctions has also been identified as an efficient strategy for enhancing the photocatalytic performance mainly via enhanced charge separation. Based on the band alignment at the interface and charge transfer between the components, as illustrated in **Figure 8**, the MHP nanocrystal heterojunctions can be classified into following types: (a) Schottky-junctions, (b) Type-II (p-n) heterojunctions, (c) all-solid-state Z-scheme heterojunction, and (d) direct Z-scheme (S-scheme) [54]. Schottky-junction (**Figure 8a**) consists of a photosensitizer to generate photoexcited electrons and a second component with more positive Fermi-energy for efficient charge separation and transfer. Type-II heterojunctions (**Figure 8b**) consist of two photocatalysts (PC I and PC II) to generate photoexcited electrons. Band alignment of PC I and PC II is such that CBM and VBM of the latter are more positive to allow electron transfer to CBM of PC II for reduction reaction and hole transfer to VBM of PC I for oxidation reaction. For Z-scheme architecture (**Figure 8c and 8d**), CBM and VBM of PC II are more negative compared to PC I, introducing a built-in electric field facilitating charge separation. Z-scheme architecture uses a high conductivity, high electron affinity electron mediator to enhance free holes in VBM of

PC I and free electrons in CBM of PC II. Direct Z-scheme utilizes spatial separation of photoexcited charge carriers through dimensionally modified structures.

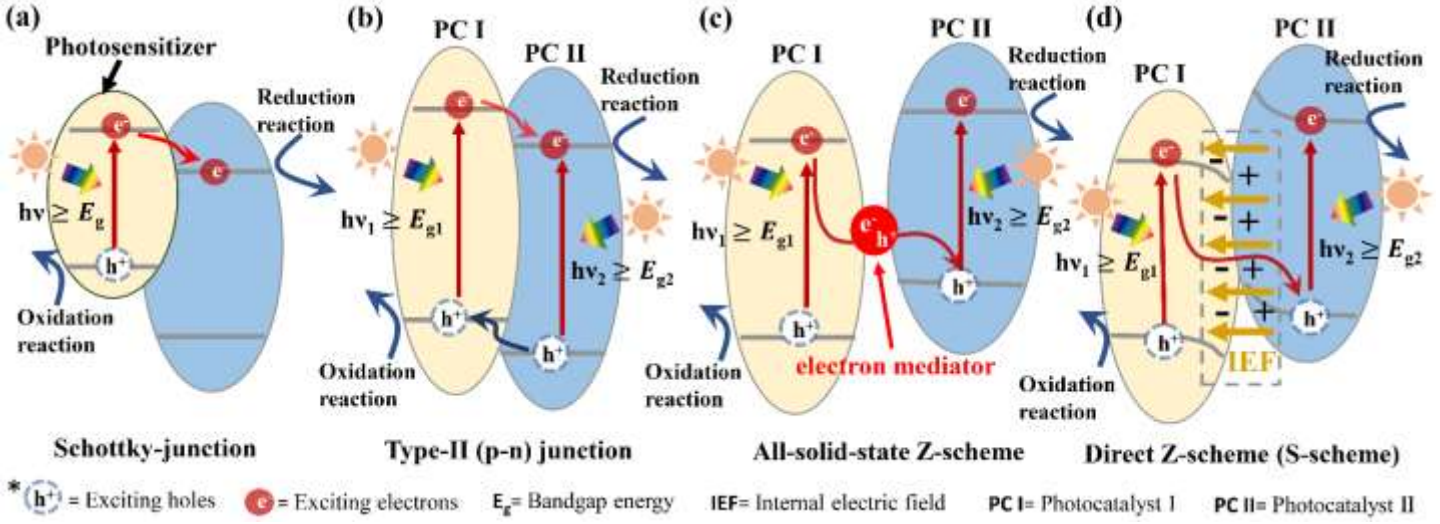

Figure 8. The typical band diagrams of heterojunctions. (a) Schottky-junction. (b) Type-II heterojunction. (c) All-solid-state Z-scheme heterojunction. (d) Direct Z-scheme (S-scheme) heterojunction.

3.2.1. Schottky Junction

In a Schottky junction device (**Figure 8a**), MHP nanocrystals act as the photosensitizer to harvest incident light, while the photogenerated electrons are extracted into the coupled functional materials (e.g., graphene oxide, metal, metal composites) for CO_2 reduction reaction. The efficient separation of the electron-hole pairs is of critical importance for MHP nanocrystals to obtain high efficiency in photocatalysis.

For example, Xu et al. [55] firstly fabricated the $CsPbBr_3$ QD/ graphene oxide nanocomposites ($CsPbBr_3$ QD/GO) as photocatalysts via a room-temperature antisolvent precipitation method. The conductive GO possessed more positive Fermi level than the conduction band edge of $CsPbBr_3$, therefore as illustrated in **Figure 9a**, the excited electrons in $CsPbBr_3$ QDs will rapidly transfer to the GO, leading to quick separation of photogenerated electron-hole pairs and suppressed charge recombination. As a result, after 12 h of photocatalytic CO_2 reduction using acetate as solvent, $CsPbBr_3$ QD/GO composites displayed a 25.5% enhancement of the rate of electron consumption (Relectron=29.8 μmol $g^{-1}h^{-1}$) compared to that of pristine $CsPbBr_3$ QD (Relectron=23.7 μmol$g^{-1}h^{-1}$). Later, Xu et al. [56] successfully developed another Schottky-junction composite for improved light-driven CO_2 reduction by attaching $CsPbBr_3$ NCs onto two-dimensional metal Pd nanosheet (**Figure 9b**). The Pd nanosheet not only served as electron reservoir to quickly separate the photogenerated electron-hole pairs in $CsPbBr_3$ NCs and suppress the undesired radiative charge recombination, but also introduced catalytic reaction sites facilitating CO_2 reduction reactions. Consequently, for the photocatalytic gaseous CO_2 reduction in the presence of H_2O vapor, the $CsPbBr_3$ NCs/Pd nanosheets composites achieved an efficient and stable electron consumption rate of 33.79 μmol $g^{-1}h^{-1}$, with a 2.43-fold enhancement over pristine $CsPbBr_3$ NC (9.86 μmol $g^{-1}h^{-1}$). Subsequently, the same group constructed the Schottky-junction using ternary composites $CsPbBr_3$ NC/BZNW/MRGO (BZNW: branched ZnO nanowire, MRGO: microporous reduced graphene oxide) for boosting photocatalytic performance toward CO_2 reduction [57]. The $CsPbBr_3$ NCs were loaded on BZNW/MRGO scaffold (**Figure 9c**) via a centrifugal cast process. The BZNW/MRGO scaffold improved electron transfer inhibiting photo-generated charge carrier recombination, exposed more active surface area for CO_2 adsorption, and enhanced the light-harvesting capacity through scattering effects. Due to these synergistic effects, a remarkable visible light-driven photocatalytic performance toward CO_2 vapor was achieved with a photoelectron consumption rate of 52.02 μmol $g^{-1}h^{-1}$, over 4.98 times higher than that of pristine $CsPbBr_3$ NCs (10.44 μmol $g^{-1}h^{-1}$). Similarly, Pan et al. [58] synthesized the functional Schottky-junction nanocomposites by the in-situ growth of $CsPbBr_3$ NCs on 2D MXene nanosheets (**Figure 9d**). The resulting $CsPbBr_3$/Mxene

nanocomposite was also demonstrated with enhanced performance in photocatalytic reduction of CO_2 in ethyl acetate solvent. Particularly, "$CsPbBr_3$ NCs/Mxene-20" nanocomposites presented high CO and CH_4 formation rates of 26.32 and 7.25 μmol $g^{-1}h^{-1}$, respectively, superior to that of pristine $CsPbBr_3$ NCs. The enhanced photo-response was also attributed to the fast separation and transfer of photogenerated carriers resulting from the conduction band offset (1.5 eV) between $CsPbBr_3$ NCs and Mxene nanosheets. The coupling of MHP nanocrystals with metal complexes is also a feasible strategy to establish Schottky-junction for visible-light-driven CO_2 reduction. As discussed in the **Section 3.1.2**, Chen et al. [45] constructed the $CsPbBr_3$-Ni(tpy) catalytic system through ligand exchange and electrostatic interactions (**Figure 9e**). In this hybrid photocatalytic system, $CsPbBr_3$ NCs acted as the photosensitizer to harvest the light, while the Ni(tpy) with metal ion cores and polypyridyl rings provided specific catalytic sites. These sites served as electron sinks to capture and store photoexcited electrons from $CsPbBr_3$ NCs, suppressing the electron-hole recombination. With the functionalization of Ni(tpy), the Schottky-junction composite $CsPbBr_3$-Ni(tpy) achieved a sharply boosted catalytic efficiency toward CO_2 reduction (1724 μmol g^{-1}) in the EA/water system, over 26-fold higher than that of pristine $CsPbBr_3$ NCs (**Figure 9f**). Kong et al. [59] adopted a similar strategy to construct the Schottky-junction nanocomposites by coordinating Re complex molecules "$Re(CO)_3Br(dcbpy)$" on the surface of $CsPbBr_3$ NCs. The strong interfacial interaction between Re complex molecules and $CsPbBr_3$ NCs resulted in a direct and fast electron transfer pathway (**Figure 9g**), which effectively integrated the high visible-light harvesting capacity of $CsPbBr_3$ and the high catalytic activity of $Re(CO)_3Br(dcbpy)$. Therefore, after loading of the Re complex molecules, the $CsPbBr_3$-$Re(CO)_3Br(dcbpy)$ composite catalyst exhibited high photocatalytic activity for the reduction of CO_2 to CO in toluene with isopropanol added as the electron donor, with the electron consumption rate (Relectron=73.34 μmol $g^{-1}h^{-1}$) 23-fold that of pristine $CsPbBr_3$ nanocrystals.

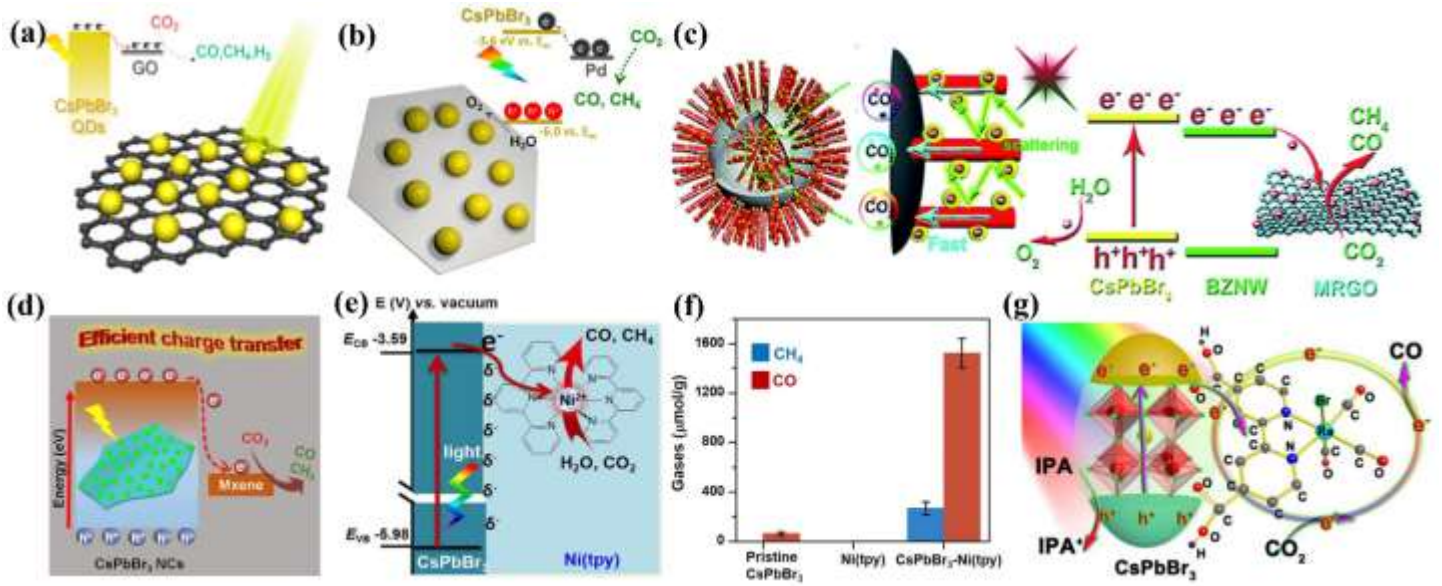

Figure 9. Schottky-heterojunctions. (a) Schematic illustration of CO_2 photoreduction over the $CsPbBr_3$ QD/GO composite photocatalyst. Reprinted with permission of Ref. 55. Copyright 2017, American Chemical Society. (b) Band alignments of the $CsPbBr_3$ NC/Pd NS composite materials and CO_2 reduction reaction over them. Reprinted with permission of Ref. 56. Copyright 2018, American Chemical Society. (c) Schematic diagram of CO_2 photoreduction over the $CsPbBr_3$ NC/BZNW/MRGO hybrids materials. Reprinted with permission of Ref. 57. Copyright 2019, The Royal Society of Chemistry. (d) Schematic illustration of $CsPbBr_3$ NCs/MXene-n heterostructures for photocatalytic CO_2 reduction. Reprinted with permission of Ref. 58. Copyright 2019, American Chemical Society. (e) The Ni(tpy) metal complexes act as electron sinks to extract exciting electrons for CO_2 reduction in the $CsPbBr_3$-Ni(tpy) photocatalyst system (f) Comparison of the photocatalytic CO_2 reduction performance of the pristine $CsPbBr_3$, the pristine Ni(tpy), and $CsPbBr_3$-Ni(tpy). Figures (e) and (f) are reprinted with permission of Ref. 45. Copyright 2020, American Chemical Society. (g) Schematic illustration of

$CsPbBr_3$-$Re(CO)_3Br(dcbpy)$ composite materials for CO_2 reduction. Reprinted with permission of Ref. 59. Copyright 2019, Wiley-VCH.

3.2.2. Type-II Heterojunctions

The formation of a type-II (p-n) heterojunction between the MHP nanocrystals and another semiconductor with proper band-edge position (e.g., g-C_3N_4, metal organic framework (MOFs), and metal oxides) could effectively boost the charge separation and thus the CO_2 reduction catalytic performance. Superior to Schottky-junctions, type-II heterojunctions theoretically exhibit higher photon utilization since both MHP nanocrystals, and the coupled semiconductor are capable of producing photoexcited charge carriers. As illustrated in **Figure 8b**, type-II heterojunction was composed of two coupled semiconductors (PC I and PC II) with staggered band. Photogenerated electrons will gather on the conduction band minimum (CBM) of photocatalyst II (PC II) for reduction reaction (e.g., CO_2 to CO/CH_4). Simultaneously, photogenerated holes will accumulate in the valence band maximum (VBM) of photocatalyst I (PC I) for oxidation reaction (e.g., H_2O to O_2). The effective spatial separation of photogenerated charge carriers and the enhanced light-harvesting capability endow the type-II heterojunction composite enhanced photocatalytic activity toward CO_2 reduction.

Ou et al. [60] anchored the $CsPbBr_3$ QDs on NH_x-rich porous g-C_3N_4 (PCN) to construct the type-II heterojunction composite via N-Br chemical bonding. As a component of the heterostructure, the g-C_3N_4 itself exhibited good properties such as reasonable visible-light response, rich surface functionality, excellent chemical stability, and promising photocatalytic activities for water splitting and CO_2 reduction. The staggered band alignment between $CsPbBr_3$ QDs and PCN effectively drove the charge separation and greatly reduced the charge recombination in the composite photocatalyst. Driven by the conduction band offset, the photogenerated electrons transferred from $CsPbBr_3$ QDs to PCN for CO_2 reduction. Meanwhile, the holes were driven from PCN to $CsPbBr_3$ QDs for H_2O oxidation by the valence band offset (**Figure 10a**). For the photocatalytic CO_2 reduction reaction carried out in acetonitrile/water mixture, the "20 CPB-PCN" composites exhibited the highest CO formation rate of 148.9 μmol $g^{-1}h^{-1}$, which was 3 times higher than pristine PCN and 15 times higher than pristine $CsPbBr_3$ QDs (<10 μmol $g^{-1}h^{-1}$). Metal-organic frameworks (MOF), also known as porous coordination polymers, represent a class of crystalline porous materials built from organic linkers and metal ions/clusters, which can behave as semiconductors and act as catalysts themselves, using open metal sites, unsaturated metal centers and catalytically active organic linkers [14,61]. Coupling MHP nanocrystals with MOF materials was proven an exceptional way to achieve a high-performance photocatalytic system for CO_2 reduction, where a type-II heterojunction was formed between them to modulate the charge transfer. For example, Kong et al. [62] demonstrated in- situ synthesis of zeolitic imidazolate framework (ZIF) on pre-formed $CsPbBr_3$ NCs templates forming $CsPbBr_3$@ZIF-8 and $CsPbBr_3$@ZIF-67 nanocomposites. The inhibited photogenerated carrier radiative recombination and effective electron transfer between $CsPbBr_3$ and ZIFs were indicated by the quenched PL intensity. The conduction band edges of both ZIF-8 and ZIF-67 were more positive than that of $CsPbBr_3$, which provided a facile charge transfer pathway for photoelectrons in $CsPbBr_3$ to ZIF. Therefore, under illumination, the photogenerated electrons in $CsPbBr_3$ will quickly transfer into ZIF, which together with the photogenerated electrons in ZIFs participated in the reduction reaction of CO_2 molecules. Meanwhile, the photogenerated holes will accumulate in $CsPbBr_3$ and quenched by H_2O molecules to generate O_2 (**Figure 10b**). In the vapor reaction mode, both $CsPbBr_3$@ZIF-8 ($R_{electron}$=15.498 μmol $g^{-1}h^{-1}$) and $CsPbBr_3$@ZIF-67 ($R_{electron}$=29.630 μmol $g^{-1}h^{-1}$) composite catalysts exhibited enhanced CO_2 reduction activity compared to that of pristine $CsPbBr_3$ ($R_{electron}$=11.142 μmol $g^{-1}h^{-1}$). The higher photocatalytic activity of $CsPbBr_3$@ZIF-67 was attributed to the active Co centers in the ZIF-67 matrix, which further reinforced the activation of reduction reaction of CO_2. Later, via a facile ultra-sonic hybrid approach, Wan et al. [63] directly coupled the pre-synthesized MOFs UiO-66(NH_2) with $CsPbBr_3$ QDs to fabricate nanocomposites, which achieved a high CO_2-to-CO conversion rate (CO generation yield of 98.57 μmol g^{-1}) in EA/water system, much higher than those of pure $CsPbBr_3$ NCs and UiO-66(NH_2). The excellent photoactivity on CO_2 reduction was ascribed to the improved electron extraction and transfer between UiO-66(NH_2) and $CsPbBr_3$ QDs (due to the formation of type-II heterojunction, **Figure 10c**), large accessible specific surface area and boosted visible-light harvesting capacity. Similarly, Wu et al. [64]

fabricated a series of composite photocatalyst of $MAPbI_3$@PCN-221(Fe_x) with x = 0 to 1, via encapsulating $MAPbI_3$ QDs in the pores of Fe porphyrin-based MOFs of PCN-211(Fe_x) for visible light-driven CO_2 reduction (**Figure 10d**). The close contact between the ligand-free $MAPbI_3$ QDs and the catalytic active center in MOFs facilitated the charge-transfer between them. Meanwhile, the photoexcited electron transfer from $MAPbI_3$ QDs to PCN-221($Fe_{0.2}$) (Fe catalytic sites) was proven to be thermodynamically permissible and the photoexcited electrons in PCN-221($Fe_{0.2}$) possessed enough driving force to reduce CO_2 to CO or CH_4. As a result, for the 25h photocatalytic CO_2 reduction reaction in EA/water system, the $MAPbI_3$@PCN-211($Fe_{0.2}$) composite photocatalysts exhibited much enhanced yield for production of CO (104 μmol g^{-1}) and CH_4 (325 μmol g^{-1}) with electron consumption rate of 112 μmol $g^{-1}h^{-1}$. It is worth noting that the $MAPbI_3$@PCN-211($Fe_{0.2}$) also exhibited obvious improved stability (80 h) due to the protection of encapsulation, accompanied by an impressive high yield of 1559 μmol g^{-1} for photocatalytic CO_2 reduction to CO and CH_4. Wang et al. [65] then constructed the $CsPbBr_3/MoS_2$ photocatalyst (CPB/MS) in the application of CO_2 photoreduction by immobilizing $CsPbBr_3$ on monolayer MoS_2 nanosheets (**Figure 10f**). A type-II heterojunction was also formed between the two components for more efficient charge separation (electrons transferred from $CsPbBr_3$ to MoS_2 nanosheets) (**Figure 10e**). Besides, the $CsPbBr_3/MoS_2$ composites showed more active sites in favor of CO_2 adsorption and activation. As a result, in the 3 h photoreduction of CO_2 in EA/water system under visible light illumination, the $CsPbBr_3/MoS_2$ (1.0 wt%) attained highest CO yield of 74.9 μmol g^{-1}, which was 2.4 times higher than that of pristine $CsPbBr_3$. Similarly, Zhang et al. [66] constructed the $CsPbBr_3$@Cu-TCPP-x type-II heterojunction composites via electrostatic assemblies of negatively charged Cu-TCPP nanosheets and positively charged $CsPbBr_3$. A strong electronic N-Pb coupling between the $CsPbBr_3$ QDs and Cu-TCPP nanosheets was demonstrated, which facilitated the migration of photogenerated electron from $CsPbBr_3$ QDs to Cu-TCPP nanosheets (**Figure 10g**) and prolonged lifetime of the charge carriers. The heterojunction composites achieved a yield of 287.08 μmol g^{-1} for the reduction of CO_2 molecules adsorbed on Cu-TCPP nanosheets during 4h reaction in acetonitrile/water solvent, over 3.87-fold improvement compared to the pristine $CsPbBr_3$ QDs.

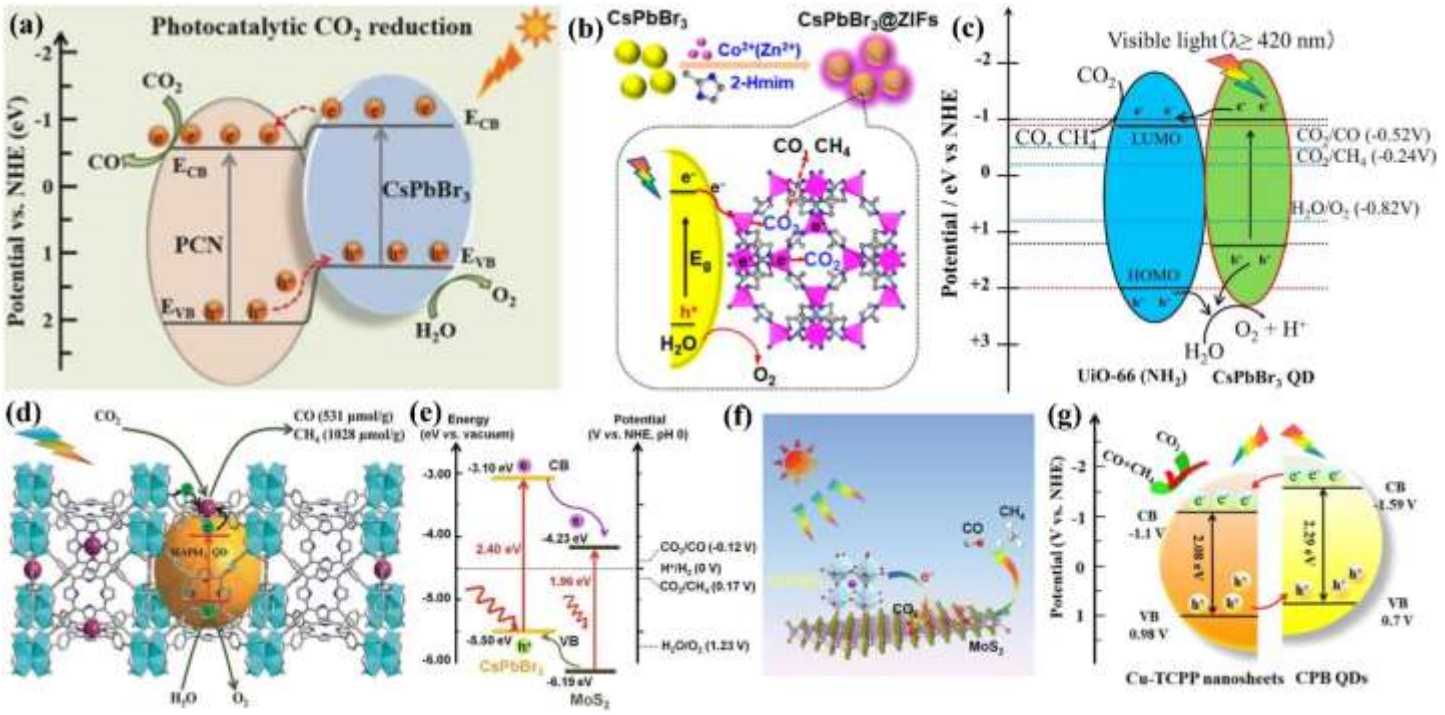

Figure 10. Type-II heterojunction. (a) Band structures of the $CsPbBr_3$ QDs/PCN composite photocatalyst. Reprinted with permission of Ref. 60. Copyright 2018, Wiley-VCH. (b) $CsPbBr_3$/ZIFs composite material for CO_2 photoreduction. Reprinted with permission of Ref. 62. Copyright 2018, American Chemical Society. (c) Schematic illustration of $CsPbBr_3$ QD/ UiO-66 (NH_2) composites for photocatalytic CO_2 reduction. Reprinted

with permission of Ref. 63. Copyright 2018, Elsevier. (d)Encapsulating $MAPbI_3$ perovskite quantum dots inside PCN-221(Fe_x) as an efficient photocatalytic system. Reprinted with permission of Ref. 64. Copyright 2019, Wiley-VCH. (e) Band diagrams of $CsPbBr_3/MoS_2$ composite photocatalyst. (f) Schematic illustration of CPB/MoS_2 photocatalytic CO_2 reduction. The (e) and (f) are reprinted with permission of Ref. 65. Copyright 2020, Elsevier. (g) Energy band structures of Cu-TCPP nanosheets/CPB QDs composite and the photocatalytic mechanism for CO_2 reduction. Reprinted with permission of Ref. 66. Copyright 2021, Elsevier.

3.2.3. Z-Scheme Heterojunction

Despite that the Schottky-junction and type-II heterojunction have been reported to effectively boost the spatial charge separation and thus the CO_2 reduction catalytic performance, the enhancement was at the cost of weakened reduction/oxidation ability of the photogenerated electron/holes due to the band offsets. On the contrary, the Z-scheme photocatalytic system was found not only facilitated the spatial separation of the photo-excited electron-hole pairs and suspended the recombination, but also reserved a strong redox capability for the photocatalytic reaction. As illustrated in **Figure 8c and d**, Z-scheme heterojunctions with a staggered band structure configuration, the photogenerated electrons in the CBM of PC I were transported to the VBM of PC II driven by the build-in voltage. Therefore, the photogenerated electrons were preserved in the CBM of PC II with strong reduction potential, while the holes accumulated in the VBM of PC I with strong oxidation potential. Simultaneously inheriting strong driving force for the redox reaction and efficient light harvesting capability by combining suitable narrow-bandgap semiconductors, the Z-scheme heterojunction composites exhibited significant superiority as the CO_2 reduction photocatalyst.

3.2.3.1. All-Solid-State Z-Scheme

Jiang et al. [67] first proposed the all-solid-state Z-scheme junction composite based on MHPs, the α-Fe_2O_3/Amine-rGO/$CsPbBr_3$, for high-efficiency photocatalytic CO_2 reduction. As illustrated in **Figure 11a**, the $CsPbBr_3$ nanocrystals were deposited on the amino-rGO coated α-Fe_2O_3 single-crystal nanorod array via a solvent evaporation-deposition process. The α-Fe_2O_3 was known as an ideal material for photocatalytic water oxidation, attributing to the inexpensive fabrication techniques, high chemical stability, and suitable band structure leading to visible-light harvesting and sufficient driving potential. The amine-rGO interlayer with high conductivity and electron affinity worked as a high-efficiency electron mediator between the α-Fe_2O_3 and $CsPbBr_3$. The built-in electric field with the direction from $CsPbBr_3$ to α-Fe_2O_3 was formed due to the large difference in their fermi level. Under illumination, the photoelectrons in the CB of α-Fe_2O_3 would be driven to recombine with the holes in the VB of $CsPbBr_3$, leaving holes in the VB of α-Fe_2O_3 while electrons in the CB of $CsPbBr_3$. The spatially separated electron-hole pairs with outstanding reduction/oxidation potential then facilitated the subsequent CO_2 reduction in the presence of H_2O. As a result, the well-designed α-Fe_2O_3/Amine-rGO/$CsPbBr_3$ exhibited a significantly advanced catalytic activity for CO_2 reduction to CO and CH_4, achieving a stable product yield of 469.16 μmol g^{-1} and an electron consumption yield of 3132.46 μmol g^{-1}. Subsequently, Mu et al. [68] developed similar all-solid-state Z-scheme heterojunction composites $CsPbBr_3$/(USGO)/ α-Fe_2O_3 by loading $CsPbBr_3$ NCs and rod-like α-Fe_2O_3 on the ultrathin and small-size graphene oxide nanosheets (USGO) (**Figure 11b**). The $CsPbBr_3$/USGO/α-Fe_2O_3 was well dispersed in the acetonitrile/H_2O solution rather anchored on the F: SnO_2 substrate as that in the study of Jiang' group [67]. The graphene oxide nanosheet also acted as the electron mediator and respectively form the C-O-Fe bonds with α-Fe_2O_3 and Br-O-C bonds with $CsPbBr_3$, accelerating the interfacial electron transfer between $CsPbBr_3$ and USGO. In this Z-scheme heterojunction, the electrons in the surface of $CsPbBr_3$ tend to migrate to α-Fe_2O_3 via USGO due to the variation in Fermi energy, resulting in a built-in electric field pointing from $CsPbBr_3$ to α-Fe_2O_3. Then the built-in electric field drove the photogenerated electrons from α-Fe_2O_3 to $CsPbBr_3$ with a Z-scheme pathway (**Figure 11c**), resulting in a facilitated charge separation and enhanced driving force for the subsequent redox reaction. The $CsPbBr_3$/USGO/ α-Fe_2O_3 composite achieved an exciting yield of 73.8 μmol $g^{-1}h^{-1}$ for CO_2-to-CO conversion, which was over 19 times higher than that of pristine $CsPbBr_3$ (3.7 μmol $g^{-1}h^{-1}$) with poor charge separation.

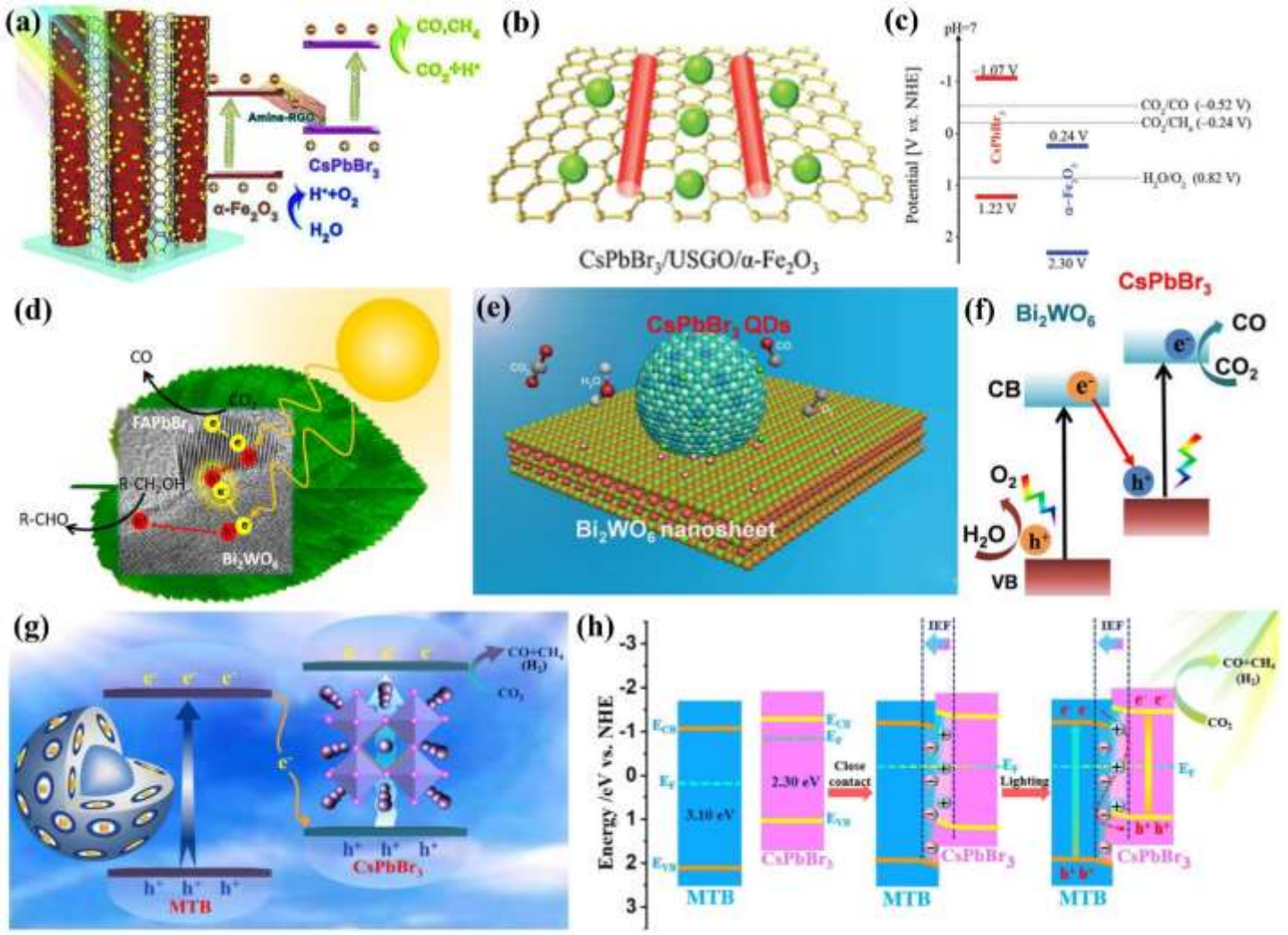

Figure 11. Z-scheme heterojunction. (a) The Z-scheme photocatalyst was fabricated via depositing $CsPbBr_3$ nanocrystals on the amine-rGO coated α-Fe_2O_3 single-crystal nanorod array. Reprinted with permission of Ref. 67. Copyright 2020, Elsevier. (b) Schematic illustration of the $CsPbBr_3$/USGO/α-Fe_2O_3 composite material. (c) Schematic illustration of band structures for $CsPbBr_3$ and α-Fe_2O_3. The (b) and (c) are reprinted with permission of Ref. 68. Copyright 2020, Wiley-VCH. (d) The CO_2 reduction reaction mechanism on the Z-Scheme photocatalyst, $FAPbBr_3/Bi_2WO_6$. Reprinted with permission of Ref. 69. Copyright 2020, American Chemical Society. (e) Schematic diagram of CO_2 photoreduction over the $CsPbBr_3$ QDs/Bi_2WO_6 nanosheet photocatalyst. (f) Band structures for the Z-scheme $CsPbBr_3$ QDs/Bi_2WO_6 nanosheet composite photocatalyst. Reprinted with permission of Ref. 70. Copyright 2020, American Chemical Society. (g) The CO_2 reduction reaction mechanism over the Z-Scheme photocatalyst, $CsPbBr_3$@MTB. (h) Schematic illustration of the $CsPbBr_3$@MTB S-scheme heterojunction. The (g) and (h) are reprinted with permission of Ref. 71. Copyright 2021, Elsevier.

3.2.3.2. Direct Z-Scheme (S-Scheme)

The above-mentioned three-component Z-scheme heterojunction not only effectively suppressed the recombination of the photogenerated electrons and holes in the narrow band gap MHP nanocrystals, but also inherited the strong energetic potential for the subsequent redox reaction, however, the unwanted light-shielding effect from the electron mediator may limit the photoactivity. Alternatively, it was better choice to directly couple MHP nanocrystals with appropriate semiconductor with properties like good visible-light response, strong interaction and staggered band structure with MHPs, and high catalytic activity for oxidation reactions. The

resultant mediator-free, direct Z-scheme (or S-scheme) photocatalytic systems exhibited faster charge transfer due to the internal electric field and avoided light shielding from the electron conductor.

For instance, Huang et al. [69] developed a S-scheme photocatalytic system based on formamidinium lead bromide and bismuth tungstate ($FAPbBr_3/Bi_2WO_6$) via antisolvent precipitation method (**Figure 11d**). The bismuth tungstate (Bi_2WO_6) possessed a suitable band gap of 2.9 eV, a relatively positive valence band (~ 3.0 eV vs RHE), and oxygen-deficient surface that exposed abundant active sites for oxidative reaction, leading to excellent photocatalytic performance in organic and water oxidations under visible light. In addition, a semi coherent interface was observed between the $FAPbBr_3$ and Bi_2WO_6, which endowed an intimate chemical and energetic interaction between them. With appropriate band structure offsets, a strong direct Z-scheme heterojunction with large driving force (2.57 eV) for the photo-redox reaction was formed. As a result, the S-scheme $FAPbBr_3/Bi2WO_6$ (12.5 wt% $FAPbBr_3$ content) photocatalyst achieved a superior CO_2 reduction rate of 170 μmol $g^{-1}h^{-1}$ under simulated solar irradiation while oxidated benzyl alcohol to value-added benzaldehyde (250 μmol $g^{-1}h^{-1}$), simultaneously. However, it was emphasized that the Z-scheme system may transform back to type-II heterojunction with diminished driving force if the content of $FAPbBr_3$ was too high (greater than 12.5 wt%), which broke the balance between the internal electric field, coulombic repulsion, and potential difference at the interface. Moreover, the organic-inorganic hybrid perovskite $FAPbBr_3$ in the composite may partially dissolve when exposed to the generated polar products, affecting the stability of the composite system. Therefore, Wang et al. [70] subsequently replaced the $FAPbBr_3$ with all inorganic perovskite $CsPbBr_3$ QDs to fabricate the $CsPbBr_3$ QDs/Bi_2WO_6 nanosheet (CPB/BWO) Z-scheme composite photocatalysts for CO_2 reduction (**Figure 11e**). The $CsPbBr_3$ QDs were decorated onto the Bi_2WO_6 nanosheets via the ultrasonic method in EA, and an intimate contact between $CsPbBr_3$ QDs and Bi_2WO_6 nanosheets was formed through the Bi-Br chemical bonds. The high-resolution X-ray photoelectron spectroscopy (HR-XPS) characterization verified the S-scheme charge migration between $CsPbBr_3$ QDs and Bi_2WO_6 nanosheets, which endowed the photocatalytic system both strong redox capability and high charge separation efficiency (**Figure 11f**). As a result, the $CsPbBr_3$-based S-scheme heterojunction photocatalyst exhibited excellent photocatalytic activity toward CO_2 reduction in EA/water solution: the total yield of CH_4/CO was 503 μmol g^{-1}, nearly 9.5 times higher than the pristine $CsPbBr_3$. Further, this composite photocatalysts showed much-improved stability, remaining 95% of its initial photocatalytic activity after four cycles of photocatalysis. Titanium dioxide (TiO_2), well known as photocatalyst for its earth abundance, low cost, nontoxicity and chemically inertness, was also employed to develop the $CsPbBr_3$-based S-scheme heterojunction for CO_2 photoreduction. Dong et al. [71] constructed the $CsPbBr_3$@mesoporous TiO_2 beads (MTB) S-scheme heterojunction by embedding $CsPbBr_3$ QDs into the pores of MTB via a self-assembly approach (**Figure 11g**). The unique MTB possessed large specific surface area and numerous active sites, which was favorable to the adsorption of CO_2 molecules and subsequent reduction reaction. In this $CsPbBr_3$@MTB composite, the interface electron transfer from $CsPbBr_3$ QDs to TiO_2 was revealed, which resulted in an internal electric field (IEF) directing from $CsPbBr_3$ to TiO_2 (**Figure 11h**). Under illumination, the IEF will drive the photoexcited electrons in TiO_2 to $CsPbBr_3$ following the S-scheme transfer pathway. The photoexcited electrons in the CB of MTB would recombine with the holes in the VB of $CsPbBr_3$, leaving oxidizing holes in the VB of MTB and reducing electrons in the CB of $CsPbBr_3$, which significantly boosted the separation of electron-hole pairs for efficient CO_2 photoreduction. As a result, the $CsPbBr_3$@MTB composite (with 15wt% $CsPbBr_3$) exhibited an electron consumption rate of 145.28 μmol $g^{-1}h^{-1}$ towards CO_2 reduction in EA/water solution, corresponding to a 3.49-fold enhancement than the pristine $CsPbBr_3$ (41.65 μmol $g^{-1}h^{-1}$). Besides, the successful encapsulation of $CsPbBr_3$ QDs in the mesopores and channels of the MTB matrix also enhanced the stability of the photocatalyst, which maintained activity after16 h cycling test.

4. Additional Issues for Application of MHPs in CO_2 Reduction

Various structure modifications in the previous section confirmed their effectiveness in improving the performance of MHPs nanocrystals for photocatalytic CO_2 reduction, however, some additional issues like the restrictions of reaction systems/platforms and the toxicity of lead still made it difficult to realize practical and large-scale application. In this section, we mainly focus on these two issues and review recent progress on them.

4.1. Reaction Systems/Platforms

4.1.1. Solid-Liquid Systems

Due to inherent ionic nature, MHP nanocrystals are extremely sensitive to moisture and unstable towards aqueous solutions or other polar solvents [72]. For example, the pristine $CsPbBr_3$ in pure water suffers quick phase transformation from $CsPbBr_3$ to $CsPb_2Br_5$ with wide bandgap, accompanied by the substantial loss in light absorption capability [73]. As a result, utilizing appropriate organic solvents to stabilize MHP nanocrystals was widely accepted in these solid-liquid photocatalytic systems (**Figure 2a**). Chen et al. [74] examined the stability and photocatalytic performance (towards CO_2 reduction) of $CsPbBr_3$ nanocrystal in several nonaqueous solvents (ethyl acetate, isopropanol, acetonitrile, dimethyl formamadium, and methanol) with various polarities, dielectric constant, and CO_2 solubilities. The $CsPbBr_3$ nanocrystals were revealed with excellent composition and phase stability in the solvents with mild polarity and proton concentration, such as toluene, ethyl acetate, isopropanol, and acetonitrile, while as expected, the $CsPbBr_3$ nanocrystals tended to dissolve in the high polarity DMF and degrade into $CsPb_2Br_5$ in methanol (**Figure 12a**). It should be mentioned that although the ethyl acetate and acetonitrile showed high solubility for CO_2 (241.0 mM in ethyl acetate and 270.0 mM in acetonitrile), the $CsPbBr_3$ nanocrystals in all these absolute solvents exhibited very limited photocatalytic activity toward CO_2 reduction, with the highest $R_{electron}$ of only 16.22 μmol g^{-1} in ethyl acetate (**Figure 12b**). Practically, the poor photocatalytic performance was attributed to the inadequate proton/electron donor in these absolute solvents. Accordingly, the organic solvents mixed with adequate amount of proton/electron source were subsequently developed as media for MHPs-based CO_2 reduction. In fact, H_2O is good proton source for photocatalytic CO_2 reduction considering the extensive source, nontoxicity, and low price, despite of the instability of MHP nanocrystals in pure water. Ingeniously, several groups developed mixtures containing organic solvents and a small quantity of H_2O, such as ethyl acetate/H_2O and acetonitrile/H_2O, which provided a stable atmosphere for the efficient photocatalytic CO_2 conversions process. For example, Ou et al. [60] evaluated their $CsPbBr_3$ QDs-based photocatalysts in both ethyl acetate/ water mixture and acetonitrile/water mixture. As shown in **Figure 12c**, in both cases the photocatalysts "20 CPB-PCN" exhibited excellent photocatalytic activity and stability, while the further higher CO evolution rates in acetonitrile/water mixture originated from the higher solubility of CO_2 in acetonitrile than that in ethyl acetate. In addition to water, some other chemicals (i.e., benzyl alcohol and methanol) can also act as the electron sacrificial reagent and get oxidized to value-added products (e.g., benzaldehyde and $HCOO^-$) during the CO_2 photocatalytic conversion [48,69]. In general, the organic solvents/electron donor mixtures were demonstrated as efficient mediums for the visible light-driven CO_2 conversion in solid-liquid system. Nevertheless, the organic reagents are typically expensive and nocuous, which are incompatible with the environmental friendliness and human security, and therefore obstruct the large-scale and commercial application. Otherwise, although a few studies realized the CO_2 photoreduction directly under pure H_2O medium via the modulation of protective structures (e.g., hexafluoro butyl methacrylate) on MHPs-based photocatalysts [75,76], the relatively low CO_2 solubility in pure water still restricted the conversion efficiency.

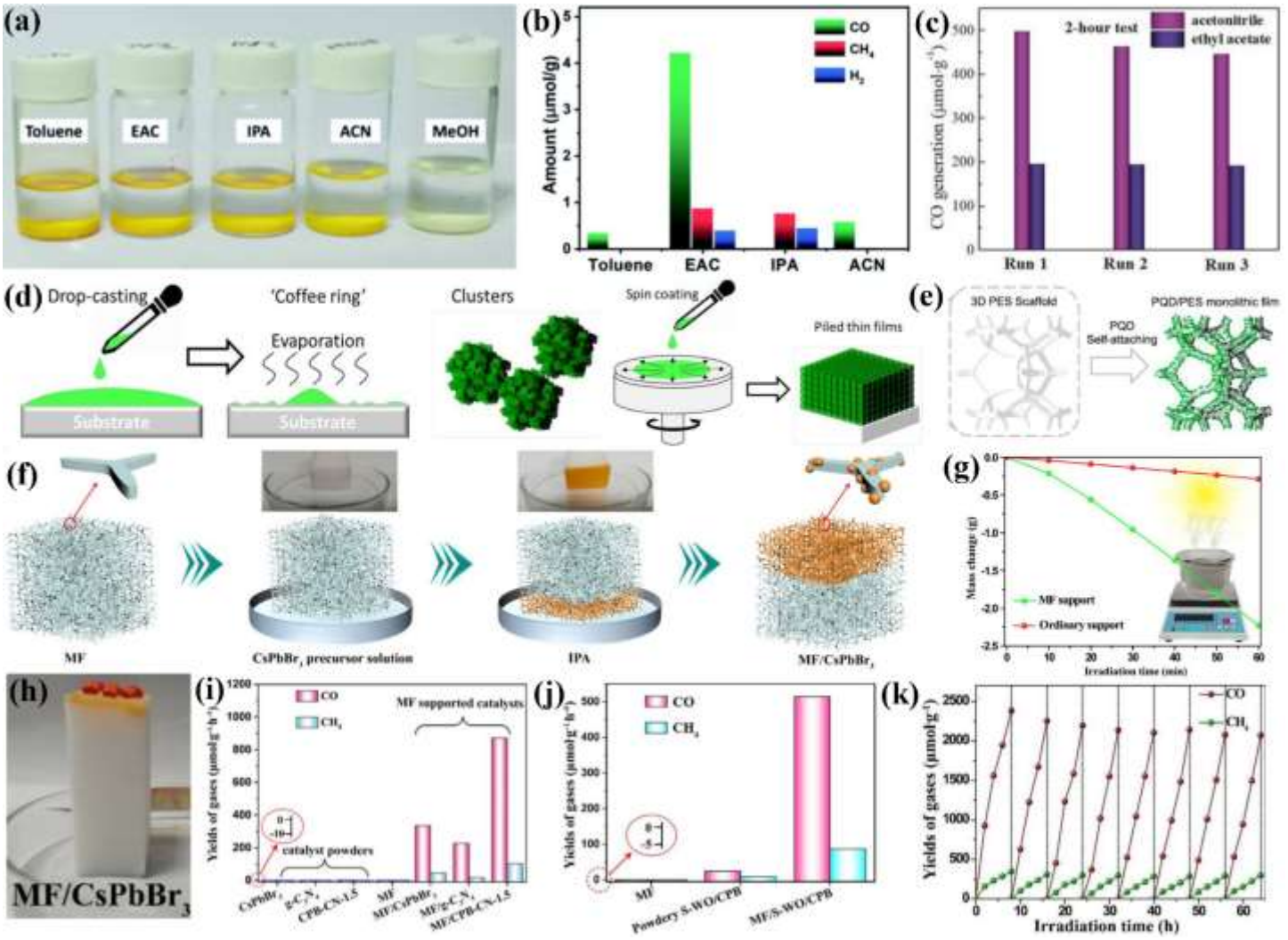

Figure 12. (a) $CsPbBr_3$ solution in various solvents after photocatalytic CO_2 reduction reaction. (b) The photocatalytic CO_2 reduction performance of $CsPbBr_3$ in various solvents. Figures (a) and (b) are reprinted with permission of Ref. 74. Copyright 2020, The Royal Society of Chemistry. (c) The CO_2 reduction performance (CO production)in acetonitrile/water and ethyl acetate/water system, respectively. Reprinted with permission of Ref. 60. Copyright 2018, Wiley-VCH. (d) Schematic illustration of drop-casting and spin-coating operation and the formation of "coffee ring" film, clusters, and stack layer, respectively. (e) Schematic illustration of self-attaching approach for QDs/PES monolithic film. Figures (d) and (e) are reprinted with permission of Ref. 46. Copyright 2021, Elsevier. (f) Schematics of $CsPbBr_3$ self-attaching on melamine foam. (g) More rapid water evaporation under the support of melamine foam. (h) Hydrophobic surface of $MF/CsPbBr_3$ which avoided direct contact with liquid H_2O. Figures (f)-(h) are reprinted with permission of Ref. 73. Copyright 2021, Wiley-VCH. (i) Photocatalytic CO_2 reduction performance of catalyst powders and MF-supported catalysts. Reprinted with permission of Ref. 77. Copyright 2021, Wiley-VCH. (j) Photocatalytic CO_2 reduction performance of pristine MF, S-WO/CPB powder and MF/S-WO/CPB, respectively. (k) Stability of MF/S-WO/CPB composite photocatalyst. Figures (j) and (k) are reprinted with permission of Ref. 78. Copyright 2021, Elsevier.

4.1.2. Solid-Vapor Systems

Alternatively, replacing organic solvent with H_2O vapor was proven as another feasible strategy for the MHPs-based photocatalytic CO_2 reduction, where the toxic and expensive organic solvents were avoided, and the reaction was carried out in a solid-vapor system (**Figure 2a**). Ideally, water vapor could sufficiently mix with high purity CO_2 and act as effective electron donor for the solid-vapor photocatalytic CO_2 reduction. A few

problems still existed in this solid-vapor system, which mainly arose from (1) the distribution/loading strategies of photocatalysts and (2) the methods to generate water vapor. Different from the solid-liquid system in which the photocatalysts were sufficiently dispersed in the solvents and fully contacted with the dissolved CO_2, in the solid-vapor system, however, the photocatalysts were typically loaded on solid substrates via strategies like drop casting, spin coating, and centrifugal coating. The excellent photocatalytic activity of the MHP nanocrystals partially derived from their high specific area, but these commonly used loading strategies usually cause stack layers or agglomerated clusters (**Figure 12d**), thus compromising the high specific area leading to poor exposure to gas reactants and detrimental charge recombination [46]. To overcome this obstacle, Cheng et al. [46] firstly developed the optimized solid-vapor photocatalytic system by loading the $CsPbBr_3$ QDs on 3D polyethersulfone (PES) scaffold with minimal agglomeration and clustering via electrostatic self-attachment (**Figure 12e**). The porous PES scaffold not only exploited the high surface/volume ratio of $CsPbBr_3$ QDs for the efficient flow-through photocatalytic reactions, but also enhanced the light harvesting through the light trapping effect resulting from the hierarchically porous structure. As a result, the perovskite quantum dots (PQD)/PES sample in this study achieved over twice production rate compared to the PQD/glass sample which was prepared by directly drop-casting the photocatalysts on a bare glass substrate. Otherwise, there are two main methods to introduce H_2O vapor in the solid-vapor photocatalytic reactor: (1) add H_2O liquor in the reactor and transit it into H_2O vapor with extra heat procedure before the photocatalytic reaction, or (2) flow the CO_2 gas through a water tank to bring moist water vapor in the reactor. Unfortunately, the former method is complex, time-consuming, laborious, and relatively costly for the large-scale application, while it is hard to guarantee sufficient concentration of H_2O vapor in the latter strategy. Most recently, Chen et al. [73] reported their innovative research in which the 3D melamine foam (MF) with an interconnected porous structure was introduced as a multifunctional assistance (**Figure 12f**). Owing to the strong H_2O adsorption and photothermal effects of the porous MF, the accelerated water evaporation was realized (**Figure 12g**) for quick and sufficient blending of CO_2 with H_2O vapor in the reactor. Besides, the MF provided a good 3D scaffold for the distribution of $CsPbBr_3$ photocatalysts and improved their moisture stability via the hydrophobic surface avoiding direct contact with liquid H_2O (**Figure 12h**). Consequently, this study provided a new platform for the highly efficient vapor-solid photocatalytic reactions. Based on this novel platform, Chen et al. [77] and Zhang et al. [78] respectively developed the MF/$CsPbBr_3$-g-C_3N_4 (**Figure 12i**) and MF/ WO/$CsPbBr_3$ (**Figure 12j**) composite photocatalysts for the CO_2 conversion with superior photocatalytic activity and stability (**Figure 12k**).

4.2. Pb-Free MHP Nanocrystals for CO_2 Reduction

Recently, Pb-based MHP nanocrystals have demonstrated huge potential in effective CO_2 conversion due to their low-cost solution processability and excellent optoelectronic properties. Nevertheless, the necessary inclusion of lead in these MHP nanocrystals raises obvious toxicity concerns, running contrary to the environmentally friendly concepts [79]. The Pb could reach the human food chain by plants from PbI_2 leakage into the ground [80], and it will do serious harm to human health, including fatigue, nausea, clumsiness, muscle weakness, and clouded consciousness [16]. Therefore, the commercialization and the widespread application of the Pb-based MHPs is difficult, and development of non-toxic MHP nanocrystals retaining the excellent properties in Pb-based MHPs is of great significance. Over the past few years, efforts have progressed greatly to develop suitable non-toxic MHP nanocrystals [81,82]. A feasible method is to replace the lead (Pb) with low-toxicity elements such as tin (Sn), germanium (Ge), bismuth (Bi), antimony (Sb), and silver (Ag) to fabricate the Pb-free metal halide perovskites (LFHPs) (**Figure 13a**). In the typical Pb-based MHPs $APbX_3$ as shown in **Figure 3a**, the Pb^{2+} cations are coordinated with six halide anions to form $[BX_6]^{4-}$ octahedra, which are connected in a corner-sharing manner and extended to a 3D framework, and the interstices among the octahedral units are occupied by the A cations with suitable ionic radius. In the case of LFHP nanocrystals, the crystal structure depends primarily on substitutions of B sites and various substitutions offer a wide diversity of crystal structures for LFHP NCs [82]. Among commonly studied Pb substitutions, only the Group 14 elements Sn and Ge can form the traditional perovskite structure ABX_3 because they both fulfil the coordination and charge balance prerequisites. However, the Sn^{2+} or Ge^{2+} undergo easy oxidation to tetravalent Sn^{4+} and Ge^{4+}, causing the

transition of a 3D ABX_3 perovskite structure to A_2BX_6. In this process, as shown in **Figure 13b**, the ordered metal vacancies form and isolate the metal halide octahedra. Replacing Pb with neighboring elements (Group 15 elements) such as Bi and Sb with higher trivalent oxidation states is another possible solution, which reduces the molecular dimensionality of perovskite crystal structure with stable stoichiometry $A_3B_2X_9$ other than the classical ABX_3. As illustrated in **Figure 13c and d**, there are mainly two polymorphs of $A_3B_2X_9$ materials: (1) The hexagonal phase consisting of zero-dimensional (0D) face-sharing bi-octahedra $[B_2X_9]^{3-}$ (dimer phase) (**Figure 13c**); (2) The two-dimensional (2D) layered perovskite structure (layered phase) of corrugated layer with partially corner sharing $[BX_6]^{3-}$ octahedra (**Figure 13d**). Moreover, substituting two lead ions with a monovalent ion (e.g., Ag^+) and a trivalent metal ion (e.g., Bi^{3+}) is an alternative, which results in the halide double perovskites $A_2B'B''X_6$ with extended three-dimensional (3D) connectivity of octahedra. Taking the Cs_2AgBiX_6 for example, as illustrated in **Figure 13e**, every pair of adjacent Pb^{2+} cations are replaced by one Ag^+ and one Bi^{3+} cation in a 3D perovskite structure. The Ag^+ and Bi^{3+} ions located on the B and B' sites are bonded with X^- to form two types of regular octahedra which then alternatively link into a face-centered cubic structure, with larger Cs^+ filling into their interstices, forming the typical cubic structure. Although there are only limited number of studies on the LFHP for photocatalytic CO_2 reduction, the reported results have highlighted their good stability obtained under ambient conditions and the excellent optoelectronic properties for CO_2 reduction. Therefore, in the section, we review the recent research progress of LFHP with different stoichiometry and crystal structures for photocatalytic CO_2 reduction.

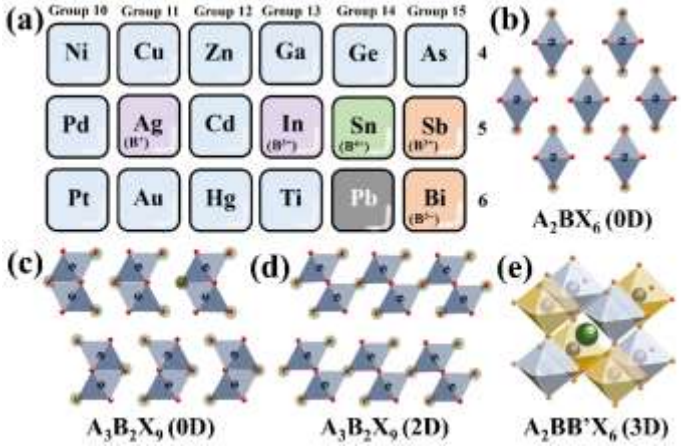

Figure 13. (a) Candidates from a part of periodic table forming Pb-free halide perovskite (LFHP) and the derivative structure for photocatalytic CO_2 conversion. Structure presentation of LFHP and perovskite derivatives showing network of octahedra in (b) 0D A_2BX_6, (c) 0D $A_3B_2X_9$, (d) 2D $A_3B_2X_9$, and (e) 3D $A_2BB'X_6$, respectively.

4.2.1. Sn-Based Halide Perovskite

The Sn- based Pb-free halide perovskite (LFHP) was the first explored analogue to Pb-based MHP NCs reported in 2016 [83]. Since the easy oxidation of Sn^{2+} to Sn^{4+}, substitution of Sn^{2+} with the more-stable Sn^{4+} has been adopted as an attractive option, resulting in the double-perovskite structure of Cs_2SnX_6 [84]. In 2019, Wang et al. successfully fabricated the Cs_2SnI_6/SnS_2 heterostructure by in-situ formation of 0D lead-free perovskite Cs_2SnI_6 on flower-like 2D SnS_2 nanosheets through co-sharing of Sn atoms and demonstrated their performance in the photocatalytic CO_2 reduction (as shown in **Figure 14a**) [85]. A typical type-II band alignment was formed in the Cs_2SnI_6/SnS_2 heterojunction while the co-shared Sn endowed the intimate contact between the two materials, both of which facilitated the transportation/separation of the charge carriers and suppressed the electron-hole recombination. The CO_2 reduction reaction was conducted in solid-vapor mode with CO_2 containing trace H_2O and CH_3OH, and the CH_4 production yield of the "Cs_2SnI_6(1.0)/SnS_2" sample showed 5.4-fold enhancement (6.09

μmol g^{-1}) comparing to the pristine SnS_2. Also, good stability of the Cs_2SnI_6/SnS_2 heterostructure was demonstrated through the 3 cycles of 3 h repeated photocatalytic reaction.

4.2.2. $A_3B_2X_9$ Nanocrystals

4.2.2.1. Bismuth (Bi)-Based $A_3Bi_2X_9$ Nanocrystals

Since the low toxicity and the high chemical stability originated from higher trivalent oxidation state, Bi is considered as a more suitable replacement for Pb than Sn. Applying Bi^{3+} to replace Pb^{2+} at the B-site results in a new type of LFHPs with $A_3Bi_2X_9$ stoichiometry. The zero-dimensional and monoclinic crystals of the $A_3Bi_2X_9$ are more likely to form surface defects, which were reported to enhance the photocatalytic activity due to increased adsorption of CO_2 and trapping of excited electrons [82]. In 2019, Diau and co-workers [86] synthesized series of $A_3Bi_2I_9$ (A=MA, Cs, and Rb) nanocrystals via a facile top-down ultrasonication method and investigated their application in photocatalytic reduction of CO_2 into CH_4 and CO. All $A_3Bi_2I_9$ nanocrystals showed better catalytic activity than TiO_2 (reference photocatalyst), and the comparative catalyst activity was observed in the order $Cs_3Bi_2I_9$ (77.6 μmol g^{-1}) > $Rb_3Bi_2I_9$ (18.2 μmol g^{-1}) > $MA_3Bi_2I_9$ (7.2 μmol g^{-1}) towards CO and $Rb_3Bi_2I_9$ (17.0±1.6 μmol g^{-1}) > $Cs_3Bi_2I_9$ (14.9±0.8 μmol g^{-1}) > $MA_3Bi_2I_9$ (9.8±0.6 μmol g^{-1}) for CH_4 evolution. Among them, $Cs_3Bi_2I_9$ had the best photocatalytic activity for the reduction of CO_2 to CH_4 as well as CO. The stability of the lead-free perovskites was also tested in severe conditions of humidity (RH=70%) and illumination, and the Bi-based perovskite showed 12 h of stability after seven days of aging under UV illumination. Later, through a modified solution recrystallization strategy, Sheng et al. [87] constructed a series of nontoxic and stable $Cs_3Bi_2X_9$ (X=Cl, Br, I) nanocrystals. Comparing to $Cs_3Bi_2Cl_9$ and $Cs_3Bi_2I_9$, $Cs_3Bi_2Br_9$ exhibited better efficiency and selectivity toward the photocatalytic reduction of CO_2-to-CO in the solid-vapor system and showed the highest CO yield of 134.76 μmol g^{-1} with 98.7% selectivity under 5 h of AM1.5G illumination. Besides, $Cs_3Bi_2Cl_9$ also presented an impressive CO yield of 83.06 μmol g^{-1} with 98.3% selectivity, which is in distinct contrast to that of 5.78 μmol g-1 in $Cs_3Bi_2I_9$. The relatively high stability of the $Cs_3Bi_2Br_9$ under long-term irradiation was also indicated with ~300 μmol g^{-1} of CO yield after 20 h of irradiation. Theoretical and experimental results demonstrated that Br endowed the $Cs_3Bi_2Br_9$ with profitable electronic band structures, enhanced solar energy utilization, promoted directional electron delivery (charge transfer), and suppressed recombination of carriers. All above attributes were favorable for efficient photocatalytic CO_2 reduction. Similar to that of Pb-based MHP nanocrystals, the construction of heterojunctions was also proved to be capable of enhancing the photocatalytic performance of the Bi-based halide perovskites, via accelerating the separation of electron-hole pairs. Liu et al. [88] successfully constructed a S-scheme heterojunction of $Cs_3Bi_2I_9/Bi_2WO_6$ composites and applied it as a photocatalyst for CO_2 reduction coupled with water oxidation. $Cs_3Bi_2I_9$ nanocrystals were in-situ grown on the surface of ultrathin Bi_2WO_6 nanosheets through co-sharing Bi atoms. The co-sharing of Bi atom enabled the intimate contact and strong electron coupling between the Bi_2WO_6 and $Cs_3Bi_2I_9$, facilitating the interfacial charge transfer. Meanwhile, a staggered band structure configuration was obtained between $Cs_3Bi_2I_9$ and Bi_2WO_6, and an internal electric field with the orientation from $Cs_3Bi_2I_9$ to Bi_2WO_6 was achieved due to the difference in their Fermi energy levels. It resulted in the Z-scheme charge transfer pathway for the photogenerated carriers in $Cs_3Bi_2I_9/Bi_2WO_6$ heterojunction, which not only realized effective charge transfer within the two components, but also possessed well-preserved redox capability (**Figure 14b**). As a result, the $Cs_3Bi_2I_9/Bi_2WO_6$ heterojunction exhibited a fourfold increase in the photocatalytic activity for the conversion of CO_2-to-CO compared with pure $Cs_3Bi_2I_9$ nanocrystals. The yield of CO reached up to 66 μmol g^{-1} for $Cs_3Bi_2I_9/Bi_2WO_6$ while just 15.2 μmol g^{-1} for pristine $Cs_3Bi_2I_9$ after 9h of irradiation. The good stability of the $Cs_3Bi_2I_9/Bi_2WO_6$ heterojunction was also proven with the three-cycling test of 6 h in the solid-vapor reaction system.

4.2.2.2. Antimony (Sb)-Based $A_3Sb_2X_9$ Nanocrystals

Antimony (Sb) is another popular trivalent substitution of Pb, and the crystal structure of the $Cs_3Sb_2Br_9$ nanocrystals also exhibits 0-D or 2-D layered structures, consistent with its bulk material. Compared to Pb-based MHP nanocrystals, defects are also more readily found in Sb-based LFHP nanocrystals. In 2020, Lu et al. [89]

successfully synthesized the uniform and pure $Cs_3Sb_2Br_9$ through the modified hot injection method. To refrain the $SbBr_3$ salt from hydrolysis (to white impurity $Sb_4O_5Br_2$ or $Sb_8O_{11}Br_2$, occurring as low as 160℃), in the hot injection synthesis process, the typically used unsaturated oleic acid (OA) was replaced by the saturated octanoic acid (OnA) to expand the synthesis temperature up to 230 ℃. After 4h reaction under illumination, the $Cs_3Sb_2Br_9$ achieved the CO production of 510 μmol g^{-1}, which exhibited a 10-fold increase in activity for the photocatalytic CO_2 reduction compared to $CsPbBr_3$ nanocrystals (50 μmol g^{-1}) (**Figure 14c**). Density functional theory calculations revealed that the key to enhancement of the activity were intermediate binding sites (COOH* and CO*) on the (1000) and (0001) surfaces of $Cs_3Sb_2Br_9$, where Sb was sufficiently exposed to allow reactivity, while the surface of pristine $CsPbBr_3$ nanocrystals was completely inert. Furthermore, the $Cs_3Sb_2Br_9$ was proven to show better stability than $CsPbBr_3$, remaining stable after 9 hours of reaction. Later, Wang et al. [90] synthesized the $Cs_3Sb_2I_9$ nanocrystals via a new vacuum in-situ crystallization method at 120 ℃. A flaky material of 200-500 nm consisting of 20 nm nanoparticles was obtained, accompanied with high crystallinity and good stability. The orange $Cs_3Sb_2I_9$ perovskite showed the absorption band edge of 607nm with the bandgap of 2.03 eV, suggesting an excellent light absorption property with suitable band position for CO_2 reduction (CBM~-1.00 eV, VBM~1.03 eV). The photothermal synergistic catalysis CO_2 reduction reaction (to CO and CH_4) was conducted in the solid-vapor reactor with trace water (50 μL) as sacrificial agents. When heated to 235 ℃, the catalytic system showed a production rate ($CO+CH_4$) of 95.7 μmol g^{-1} h^{-1} under the full spectrum illumination without co-catalysts, which was 87× and 5.2× higher than that of pure photocatalysis and pure thermal catalysis, respectively. It was demonstrated that the improvement in the activity of CO_2 reduction reaction was attributed to the synergistic effect of the thermal excitation (which produced active defect sites for CO_2 catalytic activation) and the photoexcitation (which created plentiful electrons to provide the CO_2 reduction capacity).

4.2.3. $A_2B'B''X_6$ Nanocrystals

Compared to the extended three-dimensional (3D) connectivity in lead based $APbX_3$ perovskites, the replacement of Pb by Sb or Bi can result in the lower dimensional connectivity of the octahedra (e.g., 0D-2D), leading to significant differences in the electronic properties such as higher energy band gaps, increased effective mass of charge carriers, and decreased carrier mobilities. To create LFHP nanocrystals with extended 3D connectivity, the double halide perovskites with B-site heterovalent substitution by mixed cations ($B=B^+$, $B'=B^{3+}$) is an available option. The most popular double halide perovskite is Cs_2AgBiX_6, which can be indexed to the standard cubic perovskite structure, and exhibits good stability against thermal, light, and moisture. In 2018, Zhou et al. [43] reported their successful fabrication of novel lead-free $Cs_2AgBiBr_6$ double perovskite NCs via a simple hot-injection method. The as-synthesized $Cs_2AgBiBr_6$ NCs exhibited impressive colloidal and composition stability in low polarity solution (for more than 3 weeks). Notably, even after declining the ligand density (for improved electric conductivity), $Cs_2AgBiBr_6$ NCs still maintained their superior moisture stability against 55% relatively humidity for 90d, thermal stability under 100℃ heating for 300h, or light stability under 70 mW cm^{-2} constant illumination for 500h. Owing to the suitable band positions (VBM ~6.17 eV vs. vacuum, CBM ~3.65 eV vs. vacuum, and band gap ~2.52 eV), $Cs_2AgBiBr_6$ NCs were finally applied for photochemical conversion of CO_2 into solar fuels. A total electron consumption of 105 μmol g^{-1} for CO_2 reduction to CO and CH_4 with 14.1 and 9.6 μmol g^{-1}, respectively was achieved under AM 1.5G illumination in solid-vapor mode for 6 h, displaying their great potentials as environmentally friendly halide perovskite photocatalysts. Later, Wu et al. [91] explored the effects of halide composition on the photocatalytic CO_2 reduction performance of Cs_2AgBiX_6. The lead-free mixed-halide Cs_2AgBiX_6 (X=Cl, $Cl_{0.5}Br_{0.5}$, Br, $Br_{0.5}I_{0.5}$, I) NCs were selectively synthesized via antisolvent recrystallization using isopropanol as the antisolvent, without high temperature and inert atmosphere requirements. The halide mixture enabled the Cs_2AgBiX_6 NCs with tunable absorption of visible light (e.g., absorption edges of $Cs_2AgBi(Br_{0.5}I_{0.5})_6$ and $CsAgBiI_6$ were extended to ~ 650 and ~ 680nm, respectively), with the bandgap (E_g) values ranging from 1.82 to 2.56 eV, which facilitated the utilization of visible photons for an efficient photocatalytic system. Owing to the appropriate band gaps and desirable band edge alignment, $Cs_2AgBiCl_6$, $Cs_2AgBi(Br_{0.5}I_{0.5})_6$, and Cs_2AgBiI_6 NCs were selected as the photocatalysts for CO_2 reduction (to CO) in gas-

solid mode. After constant irradiation of visible light for 3h, Cs_2AgBiI_6 displayed the highest photoreduction activity with a CO yield of 18.9 μmol g^{-1} and 100% selectivity, indicating an electron consumption of 37.8 μmol g^{-1}. Meanwhile, $Cs_2AgBiCl_6$ and $Cs_2AgBi(Bi_{0.5}I_{0.5})I_6$ also presented CO yields of 13.62 and 11.88 μmol g^{-1}, respectively. The author emphasized that the yield of CO using Cs_2AgBiI_6 for 3h photocatalytic CO_2 reduction in this work was higher than that of $Cs_2AgBiBr_6$ for 6h in Zhou et al.'s work [43] (14.1 μmol g^{-1}, without ligands washing). Improved photocatalytic performance was attributed to the wider light absorption range (higher utilization of visible light photons) and better band alignment resulting from the halide-mixture tunning. Morphology control was also proven as an important strategy for tuning the performance of the functional nanomaterials. Liu et al. [92] reported successful synthesis of high-quality Cs_2AgBiX_6 (X=Cl, Br, I) 2D nanoplatelets (NPLs) through a newly developed synthetic procedure, which possessed a better performance in photocatalytic CO_2 reduction compared with their nanocube counterpart due to the shape effect (**Figure 14d**). Both the CO and CH_4 production rates were significantly higher when using NPLs as catalysts compared to the NCs. The total electron consumption during the 6 h reaction for $Cs_2AgBiBr_6$ NPLs showed a more than 8× enhancement compared to $Cs_2AgBiBr_6$ NCs (255.4 μmol g^{-1} vs 30.8 μmol g^{-1}). The author attributed the dramatical improvement in the photocatalytic performance to the anisotropically confined charge carriers and their in-plane long diffusion length for the NPLs as compared to their NC counterparts. Moreover, the superior material stability of $Cs_2AgBiBr_6$ NPLs were demonstrated as crystal structure and 2D morphology was maintained after the photoreaction. $Cs_2AgInCl_6$ is another example of the double perovskite quantum dots applied in the photocatalytic CO_2 reduction, which replace two Pb^{2+} with monovalent (Ag^+) and trivalent (In^{3+}) metal ions to form a quaternary double perovskite, maintaining the high structural (and possibly electronic) dimension of the perovskite lattice. Chen et al. [44] synthesized the Ag-loaded lead-free $Cs_2AgInCl_6$ QD ($Cs_2AgInCl_6$ QD@Ag) composites by the hot-injection method and applied these composites for photocatalytic CO_2 reduction (**Figure 14e**). The loading of the Ag nanoparticles greatly improved the poor light absorption performance (large bandgap of 4.88 eV) of the bare $Cs_2AgInCl_6$ due to the surface plasmon resonance (SPR) effect of Ag nanoparticles, which generated extra hot electron on Ag surface under visible light irradiation. As a result, all the tested $Cs_2AgInCl_6$ QD@Ag composites possessed excellent photocatalytic activity, and the $Cs_2AgInCl_6$ QD@Ag-2 composite purified with process II exhibited the highest performance. The yields of CO and CH_4 reached 26.4 and 28.9 μmol g^{-1}, respectively, after simulated illumination for 3h. Further, reasonable photocatalytic and phase stability of the $Cs_2AgInCl6$ QD@Ag-2 was also demonstrated with minimal decline (decrease of 5.4%) of CO_2 photoreduction performance cycling test for 9h.

4.2.4. Additional Pb-free Halide Perovskites

In addition to conventional LFHPs, some earth abundant B-cations have recently shown promise for photocatalytic CO_2 reduction. Sheng et al. [93] have demonstrated Cu^{2+}-based halide perovskite Cs_2CuBr_4 QDs synthesized via an improved antisolvent recrystallization method. Attributed to the surface-frustrated Lewis pair sites (Lewis acid Cu^{2+} and base Br^- with appropriate spatial isolation, as shown in **Figure 14f**) and the intrinsic Cu d-band properties, Cs_2CuBr_4 QDs exhibited highly efficient CO_2 adsorption and activation ability. As a result, an excellent photocatalytic CO_2 reduction performance of Cs_2CuBr_4 QDs was exhibited, with the CH_4 and CO yields of 74.81 and 148.98 μmol g^{-1} in the 5h reaction in the solid-vapor reaction system, which were much higher than that of the pristine $CsPbBr_3$ QDs (CO production rate of 18.24 μmol g^{-1} and nearly no CH_4 produced). Moreover, it is noteworthy that the Cs_2CuBr_4 QDs also hold good long-term photocatalytic stability, as negligible degradation in the product yield was observed after reaction for 20h. Subsequently, Zhao et al. [94] demonstrated Cu^{2+}-based 1D rod-like halide perovskite $CsCuCl_3$ microcrystals (MCs), as illustrated in **Figure 14g**, prepared via facile antisolvent recrystallization method. $CsCuCl_3$ microcrystals possess an appropriate bandgap (1.92 eV) for effectively harvesting the sunlight and negative enough CBM potential to thermodynamically drive the CO_2 reduction (to CH_4 and CO). In the solid-liquid CO_2 reduction system using EA as solvent and IPA as "hole scavenger", $CsCuCl_3$ MCs exhibited yields of 2.79 μmol g^{-1} for CO and 11.55 μmol g^{-1} for CH_4 in short-term 3 h photocatalytic reaction, with the electron consumption rate ($E_{electron}$) of 32.66 μmol $g^{-1}h^{-1}$. Furthermore, Cl^- anions in the $CsCuCl_3$ MC can be partially substituted by Br^- to form the $CsCuCl_2Br$ MCs with narrower bandgap

and better charge carrier transfer efficiency. As a result, the $CsCuCl_2Br$ MCs showed relatively higher production yields of CO (5.61 μmol $g^{-1}h^{-1}$) and CH_4 (15.36 μmol $g^{-1}h^{-1}$) in the short-term 3 h CO_2 reduction reaction, corresponding to a $R_{electron}$ of 44.71 μmol $g^{-1}h^{-1}$. The authors also emphasized that both $CsCuCl_3$ MCs and $CsCuCl_2Br$ MCs hold good long-term photocatalytic stability and showed product yields of 103.9 and 153.4 μmol g^{-1} in 20 h reaction.

In addition to Cu-based halide perovskite, Tian et al. [95] reported their cutting-edge work on novel lead-free perovskite Cs_2XCl_6 (X=Hf, Zr, Te) microcrystals for photocatalytic CO_2 reduction [95]. Three kinds of lead-free Cs_2XCl_6 (X= Hf, Zr, Te) perovskite MCs were synthesized via the solvothermal synthesis method. As shown in **Figure 14h**, in the solid-vapor CO_2 reduction system with glass slide as substrate, the Cs_2TeCl_6 MCs showed the best photocatalytic performance with CO yield of 284.4 μmol g^{-1} at electron consumption of 568.8 μmol g^{-1} and CH_4 yield of 48.96 μmol g^{-1} at electron consumption of 391.7 μmol g^{-1} in the 3 h reaction. Meanwhile, the Cs_2HfCl_6 (CO yield of 204.3 μmol g^{-1}, and CH_4 yield of 48.66 μmol g^{-1}) and Cs_2ZrCl_6 (CO yield of 219.2 μmol g^{-1}, and CH_4 yield of 48.36 μmol g^{-1}) also exhibited good reaction activity. Moreover, the excellent air, light, and thermal stability of the Cs_2TeCl_6 MCs was also verified.

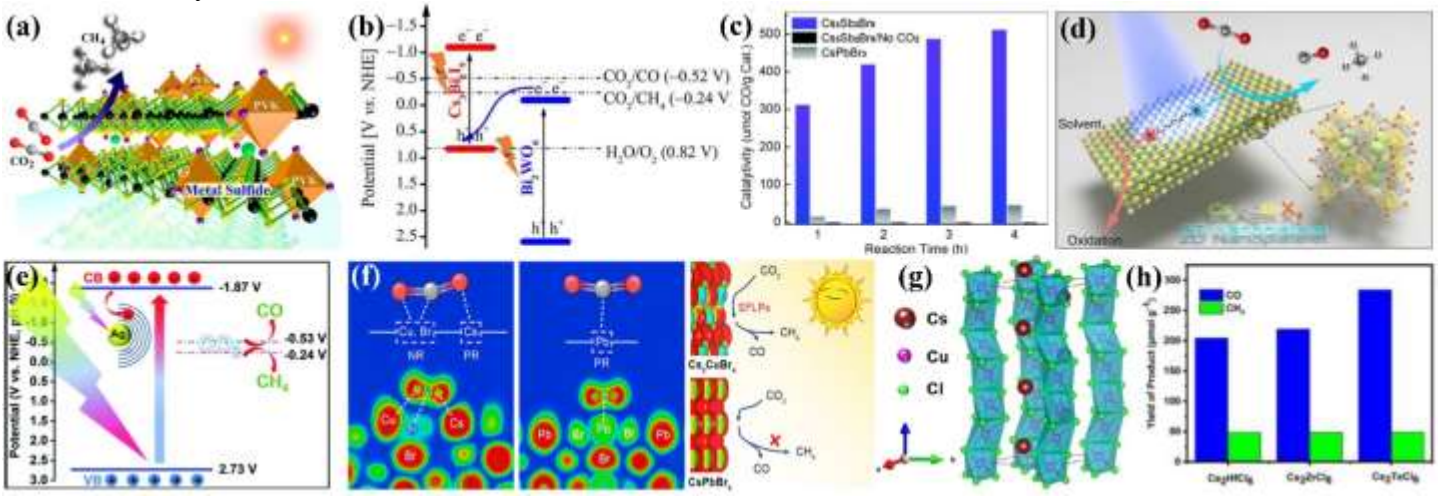

Figure 14. LFHP nanocrystals for photocatalytic CO_2 reduction. (a) Schematic illustration of Cs_2SnI_6/SnS_2 for photocatalytic CO_2 reduction. Reprinted with permission of Ref. 85. Copyright 2019, American Chemical Society. (b) Band structure for $Cs_3Bi_2I_9/Bi_2WO_6$ composite photocatalyst. Reprinted with permission of Ref. 88. Copyright 2021, Wiley-VCH. (c) Photocatalytic CO_2 reduction performance (CO production) of $Cs_3Sb_2Br_9$ NCs, with $CsPbBr_3$ NCs as a reference. Reprinted with permission of Ref. 89. Copyright 2020, The Royal Society of Chemistry. (d) Schematic illustration of the $Cs_2AgBiBr_6$ NPL for CO_2 photocatalytic reduction reaction. Reprinted with permission of Ref. 92. Copyright 2021, American Chemical Society. (e) Bandgap structure of the CAIC QDs@Ag composite. Reprinted with permission of Ref. 44. Copyright 2021, The Royal Society of Chemistry. (f) The effect of the surface-frustrated Lewis pairs (SFLP) site on CO_2 molecular absorption configuration and CO_2 photocatalytic reduction reaction performance. Reprinted with permission of Ref. 93. Copyright 2022, American Chemical Society. (g) Crystal structure of the 1D rod-like $CsCuCl_3$. Reprinted with permission of Ref. 94. Copyright 2022, American Chemical Society. (h) The photocatalytic CO_2 reduction performance of Cs_2HfCl_6, Cs_2ZrCl_6, and Cs_2TeCl_6 MCs, respectively. Reprinted with permission of Ref. 95. Copyright 2022, Elsevier.

5. Conclusion and Outlook

The advantages of MHP nanocrystals in photocatalysis application benefit from their outstanding properties, such as excellent electrical and optical properties, easy fabrication, low cost, tunable structure, dimensionality, and morphology. In this review, the up-to-date advances and achievements related to photocatalytic CO_2 reduction of MHP nanocrystals are reviewed and the corresponding photocatalytic activities are summarized in **Table 1**. First, the structural modifications of MHP nanocrystals for enhanced photocatalytic CO_2 reduction are highlighted,

which are mainly in two directions: (1) Direct modulation of the pristine MHP nanocrystals such as morphology/dimensionality, surface and composition engineering; (2) Integrating pristine MHP nanocrystals with other suitable functional materials to construct heterojunctions, including Schottky-junctions, Type-II (p-n), Z-scheme and S-scheme heterojunctions. All these strategies significantly improved the performance of the MHP nanocrystals based photocatalysts for CO_2 conversion. Subsequently, we lay particular emphasis on the issues obstructing MHP nanocrystals based photocatalysis from practical application, relating to reaction systems/platforms (solid-liquid systems or solid-vapor systems) and especially the toxicity Pb. Replacing the Pb with non-toxic elements is indeed a practical solution to break the main bottlenecks of Pb-based MHPs in photocatalytic CO_2 reduction. The Pb-free halide perovskite (LFHP) nanocrystals were demonstrated to hold better stability than Pb-based halide perovskite nanocrystals while exhibiting comparable or better photocatalytic activity for CO_2 reduction. Therefore, more future efforts should focus on the exploration of LFHP nanocrystals and their application in photocatalytic CO_2 reduction. The optimization strategies widely applied in Pb-based MHP nanocrystals like composition tuning, morphology control, and formation of heterostructures were also demonstrated as effective methods to further improve the photocatalytic activity of LFHPs. Metal halide perovskites offer excellent properties for photocatalysis of CO_2, but improvements are needed for stability and the development of effective catalysts. Pb-free MHPs catalysts are in nascent stage of research with huge prospects for composition engineering, heterojunction construction, and reaction systems towards stable, earth-abundant and sustainable materials for photocatalytic solar fuel generation.

Table 1. Recent Advances and Achievements Applying MHPs Nanocrystals Photocatalysts for CO_2 Reduction

No.	Photocatalysts	Reaction system	Light Source	Productivity	Stability	Ref.
1	$CsPbBr_3$ NCs	Solid-Liquid (EA/H_2O)	300 W Xe lamp	8.5 nm $CsPbBr_3$ nanocrystal 34.1±0.1 μmol g^{-1} for CO (8h) 12.2±0.1 μmol g^{-1} for CH_4 (8h) 0.8±0.03 μmol g^{-1} for H_2 (8h)	Reaction stability > 8 h	[30]
2	$CsPbX_3$ (X=Br, I) nanosheets	Solid-Vapor	300W Xe lamp (100 mW cm^{-2})	a. $CsPbBr_3$ nanocrystals: 5.7 μmol $g^{-1}h^{-1}$ for CO b. 4 nm $CsPbBr_3$ nanosheets: 21.6 μmol $g^{-1}h^{-1}$ for CO c. 4 nm $CsPbBr_{2.4}I_{0.6}$ nanosheets: 43.9 μmol $g^{-1}h^{-1}$ for CO	Reaction stability > 30 h	[36]
3	$CsPbBr_3$ nanocrystals	Solid-Liquid (EA/H_2O)	450 W Xe-lamp (150 mW cm^{-2})	a. Cube-shaped $CsPbBr_3$ nanocrystals: 16.4 μmol g^{-1} for CO (4h) 7.6 μmol g^{-1} for CH_4 (4h) b. Hexapod $CsPbBr_3$ nanocrystals: 79.5 μmol g^{-1} for CO (4h) 38.4 μmol g^{-1} for CH_4 (4h) c. Polyhedrons $CsPbBr_3$ nanocrystals: 130.7 μmol g^{-1} for CO (4h) 58.8 μmol g^{-1} for CH_4 (4h)	Reaction stability > 6 h	[37]
4	Surface Pb-rich $CsPbCl_3$ QDs	Solid-Liquid (Pure H_2O)	AM 1.5G solar light (150 mW cm^{-2})	a. Ni: $CsPbCl_3$ nanocrystals: 8.55 μmol $g^{-1}h^{-1}$ for CO b. Pb-rich Ni: $CsPbCl_3$ nanocrystals: 169.37 μmol $g^{-1}h^{-1}$ for CO c. Pb-rich Mn: $CsPbCl_3$ nanocrystals: 152.49 μmol $g^{-1}h^{-1}$ for CO	Reaction stability > 3 h	[40]
5	$Cs_2AgBiBr_6$ nanocrystals	Solid-Liquid (Solute EA)	AM 1.5G 100 W Xe-lamp (150 mW cm^{-2})	a. Washed $Cs_2AgBiBr_6$ NCs: 14.1 μmol g^{-1} for CO (6h) 9.6 μmol g^{-1} for CH_4 (6h) b. As-prepared $Cs_2AgBiBr_6$ NCs: 5.5 μmol g^{-1} for CO (6h) 0.65 μmol g^{-1} for CH_4 (6h)	Moisture stability ≥90 d (RH=55%, 25°C) Thermal stability ≥300 h (100°C, N_2) Illumination stability	[43]

					≥500 h (70 mW cm^{-2})	
6	$CsPbBr_3$-Ni(tpy)	Solid-Liquid (EA/H_2O)	300W Xe-lamp (100 mW cm^{-2})	a. $CsPbBr_3$-Ni(tpy) composites: 1464 μmol g^{-1} for CO (4h) 260 μmol g^{-1} for CH_4 (4h) b. Pristine $CsPbBr_3$ nanocrystals: <100 μmol g^{-1} for CO (4h)	Reaction stability > 16h	[45]
7	$CsPbI_xBr_{3-x}$/PES	Solid-Vapor (PES as scaffold)	AM 1.5 G 1sun condition solar simulator	a. $CsPbBr_3$ QDs/Glass: 11.87 μmol g^{-1} h^{-1} for CO b. $CsPbBr_3$ QDs/PES: 27.22 μmol g^{-1} h^{-1} for CO c. $CsPbI_{2.6}Br_{0.39}$ QDs/PES: 32.45 μmol g^{-1} h^{-1} for CO	Reaction stability > 2h	[46]
8	$Co_{1\%}$@$CsPbBr_3$/Cs_4PbBr_6	Solid-liquid (ACN/H_2O/CH_3OH)	300W Xe-lamp 100mW cm^{-2}	a. $Co_{1\%}$@$CsPbBr_3$/Cs_4PbBr_6: 1835 μmol g^{-1} for CO (15h) b. $CsPbBr_3$/Cs_4PbBr_6: 678 μmol g^{-1} for CO (15h)	Reaction stability > 15h	[48]
9	Fe: $CsPbBr_3$	Solid-liquid (EA/H_2O)	450 W Xe-lamp 150mW cm^{-2}	a. $Fe_{3\%}$: $CsPbBr_3$: 3.2 μmol g^{-1} h^{-1} for CO 6.1 μmol g^{-1} h^{-1} for CH_4 b. Pristine $CsPbBr_3$: 4.6 μmol g^{-1} h^{-1} for CO 1.9 μmol g^{-1} h^{-1} for CH_4	Reaction stability > 3h	[49]
10	Mn:CsPb(Br/Cl)	Solid-liquid (EA)	300W Xe-lamp 1.5 Am	a. Mn:CsPb(Br/Cl): 1917 μmol g^{-1} for CO (9h) 82 μmol g^{-1} for CH_4 (9h) b. Pristine $CsPbBr_3$ 135 μmol g^{-1} for CO (9h) 58.6 μmol g^{-1} for CH_4 (9h)	Reaction stability > 9h	[50]
11	Ni:$CsPbBr_{2.77}Ac_{0.23}$ NCs	Solid-vapor	300W Xe-lamp 100mW cm^{-2}	a. Ni: $CsPbBr_{2.77}Ac_{0.23}$: 44.09 μmol g^{-1} h^{-1} for CO b. Ni: $CsPbBr_3$: 14.49 μmol g^{-1} h^{-1} for CO c. Pristine $CsPbBr_3$: 5.03 μmol g^{-1} h^{-1} for CO	Reaction stability > 18h	[53]
12	$CsPbBr_3$ QDs/GO composite	Solid-liquid (pure EA)	100W Xe lamp AM 1.5 G	a. $CsPbBr_3$ QDs/GO composite: $R_{electron}$ = 29.8 μmol g^{-1} h^{-1} b. Pristine $CsPbBr_3$ QDs: $R_{electron}$ = 23.7 μmol g^{-1} h^{-1}	Reaction stability > 12h	[55]
13	$CsPbBr_3$ NC/Pd NS	Solid-vapor	150W Xe-lamp (420 nm filter) 150 mW cm^{-2}	a. $CsPbBr_3$ NC/Pd NS (600): $R_{electron}$ = 33.79 μmol g^{-1} h^{-1} b. Pristine $CsPbBr_3$ QDs: $R_{electron}$ = 9.86 μmol g^{-1} h^{-1}	Reaction stability > 9h	[56]
14	$CsPbBr_3$ NC/BZNW/ MRGO	Solid-vapor	150 W Xe-lamp AM1.5G (420 nm filter) 150mW cm^{-2}	a. $CsPbBr_3$ NC/BZNW/MRGO: $R_{electron}$ = 52.02 μmol g^{-1} h^{-1} b. $CsPbBr_3$ NC/ MRGO: $R_{electron}$ = 31.52 μmol g^{-1} h^{-1} c. Pristine $CsPbBr_3$ NC: $R_{electron}$ = 10.44 μmol g^{-1} h^{-1}	Reaction stability > 12h	[57]
15	$CsPbBr_3$ NCs/MXene nanocomposites	Solid-liquid (pure EA)	300W Xe-lamp (420 nm filter)	a. $CsPbBr_3$/MXene-20: 133.05 μmol g^{-1} for CO (5h) 33.83 μmol g^{-1} for CH_4 (5h) b. Pristine $CsPbBr_3$: 49.50 μmol g^{-1} for CO (12h) 22.90 μmol g^{-1} for CH_4 (12h)	Reaction stability > 5h	[58]
16	$CsPbBr_3$-$Re(CO)_3Br$(dcbpy) composite	Solid-liquid (Toluene/isopropanol)	AM 1.5 G 150 mW cm^{-2} (420 nm filter)	a. $CsPbBr_3$-Re(600): $R_{electron}$ = 73.34 μmol g^{-1} h^{-1} b. Pristine $CsPbBr_3$ $R_{electron}$ = 3.19 μmol g^{-1} h^{-1}	Reaction stability > 15h	[59]
17	$CsPbBr_3$ QDs/ PCN	Solid-liquid (ACN/H_2O or EA/H_2O)	300 W Xe-lamp (420 nm filter)	a. 20 CPB-PCN: 148.9 μmol g^{-1} h^{-1} for CO in ACN/H_2O	Reaction stability	[60]

				b. Pristine $CsPbBr_3$ QDs: <10 μmol g^{-1} h^{-1} for CO in ACN/H_2O	> 6h	
18	$CsPbBr_3$@ZIF composites	Solid-vapor	100W Xe-lamp AM 1.5G 150mW cm^{-2}	a. $CsPbBr_3$@ZIF-67: $R_{electron}$ = 29.630 μmol g^{-1} h^{-1} b. $CsPbBr_3$@ZIF-8: $R_{electron}$ = 15.498 μmol g^{-1} h^{-1} c. Pristine $CsPbBr_3$ QDs: $R_{electron}$ = 11.14 μmol g^{-1} h^{-1}	Reaction stability > 18 h Moisture stability >10 days	[62]
19	$CsPbBr_3$ QDs/UiO-66(NH_2) nanocomposites	Solid-liquid (EA/H_2O)	300 W Xe-lamp (420 nm filter)	15%-$CsPbBr_3$ QDs/UiO-66(NH_2): 98.57 μmol g^{-1} for CO (12h) 3.08 μmol g^{-1} for CH_4 (12h)	Reaction stability > 36h	[63]
20	$MAPbI_3$@PCN-221(Fe_x)	Solid-liquid (EA/H_2O)	300W Xe lamp (400 nm filter) 100 mW cm^{-2}	MAPbI3@PCN-211 ($Fe_{0.2}$) composite: 104 μmol g^{-1} for CO (25h) 325 μmol g^{-1} for CH_4 (25h) 530.06 μmol g^{-1} for CO (80h) 1028.94 μmol g^{-1} for CH_4 (80h)	Reaction stability > 80h	[64]
21	$CsPbBr_3$/MoS_2 composites	Solid-liquid (EA/H_2O)	300 W Xe lamp (420 nm filter) 200 mW cm^{-2}	a. CPB/MS (1.0 wt%): 74.9 μmol g^{-1} for CO (3h) b. Pristine $CsPbBr_3$ 31.2 μmol g^{-1} for CO (3h)	Reaction stability > 30h	[65]
22	$CsPbBr_3$@Cu-TCPP composites	Solid-liquid (ACN/H_2O)	300 W Xe-lamp (420 nm filter)	a. CPB@Cu-TCPP-20: 287.08 μmol g^{-1} for CO (4h) 3.25 μmol g^{-1} for CH_4 (4h) b. Pristine $CsPbBr_3$ QDs: 74.18 μmol g^{-1} for CO (4h)	Reaction stability > 16h	[66]
23	α-Fe_2O_3/Amine-RGO/$CsPbBr_3$	Solid-vapor	AM 1.5G (420 nm filter) 150 mW cm^{-2}	a. α-Fe_2O_3/Amine-RGO/$CsPbBr_3$: 35.47 μmol g^{-1} for CO (15h) 141.81 μmol g^{-1} for CH_4 (15h) 4.36 μmol g^{-1} for H_2 (15h) b. α-Fe_2O_3/ $CsPbBr_3$: 21.05 μmol g^{-1} for CO (15h) 43.17 μmol g^{-1} for CH_4 (15h) 2.42 μmol g^{-1} for H_2 (15h) c. Pristine $CsPbBr_3$ nanocrystal: 16.23 μmol g^{-1} for CO (15h) 14.32 μmol g^{-1} for CH_4 (15h)	Reaction stability > 40h	[67]
24	$CsPbBr_3$/USGO/α-Fe_2O_3	Solid-liquid (ACN/H_2O)	100 mW cm^{-2} (420 nm filter)	a. CsPbBr3/USGO/ α-Fe_2O_3: 73.8 μmol g^{-1} h^{-1} for CO b. Pristine $CsPbBr_3$ nanocrystal: 3.7 μmol g^{-1} h^{-1} for CO	Reaction stability > 16h	[68]
25	$FAPbBr_3$/Bi_2WO_6	Solid-liquid (Trifluorotoluene)	150 W Xe-lamp AM 1.5 G filter 100 mW cm^{-2}	12.5 wt% $FAPbBr_3$/Bi_2WO_6: 170 μmol g^{-1} h^{-1} for CO 250 μmol g^{-1} h^{-1} for benzyl alcohol (BA) to benzaldehyde (BD) conversion	Reaction stability > 20h	[69]
26	$CsPbBr_3$ QDs/Bi_2WO_6 nanosheet	Solid-liquid (EA/H2O)	300 W Xe-lamp 100 mW cm^{-2} (400 filter)	a. CPB/BWO-5: 503 μmol g^{-1} for CO+ CH_4 (10h) b. Pristine $CsPbBr_3$ QDs: 52.95 μmol g^{-1} for CO+ CH_4 (10h)	Reaction stability > 10h	[70]
27	$CsPbBr_3$@MTB composites	Solid-liquid (EA/H_2O)	300 W Xe-lamp AM 1.5 filter	a. 15wt% $CsPbBr_3$@MTB composite: 145.28 μmol g^{-1} h^{-1} for CO b. Pristine $CsPbBr_3$ QDs: 41.65 μmol g^{-1} h^{-1} for CO	Reaction stability > 16h	[71]
28	MF/$CsPbBr_3$	Solid-vapor (MF as scaffold)	300W Xe-lamp AM 1.5 G	a. MF/$CsPbBr_3$: 29.13 μmol g^{-1} h^{-1} for CO 12.95 μmol g^{-1} h^{-1} for CH_4 b. Pristine $CsPbBr_3$ on ordinary support: 11.59 μmol g^{-1} h^{-1} for CO 2.66 μmol g^{-1} h^{-1} for CH_4	Reaction stability > 104h	[73]
29	MF/$CsPbBr_3$/g-C_3N_4	Solid-vapor (MF as scaffold)	300W Xe-lamo (without filter)	a. MF/CPB/CN-1.5: 872.22 μmol g^{-1} h^{-1} for CO 103.35 μmol g^{-1} h^{-1} for CH_4	Reaction stability > 76h	[77]

				b. MF/$CsPbBr_3$: 333.88 μmol g^{-1} h^{-1} for CO 44.97 μmol g^{-1} h^{-1} for CH_4 c. MF/g-C_3N_4: 227.37 μmol g^{-1} h^{-1} for CO 17.11 μmol g^{-1} h^{-1} for CH_4		
30	MF/WO/$CsPbBr_3$	Solid-vapor (MF as scaffold)	300W Xe-lamp	a. MF/S-WO/CPB: 514.06 μmol g^{-1} h^{-1} for CO 86.56 μmol g^{-1} h^{-1} for CH_4 b. MF/CPB: 332.17 μmol g^{-1} h^{-1} for CO 43.16 μmol g^{-1} h^{-1} for CH_4 c. MF/S-WO_3: 149.67 μmol g^{-1} h^{-1} for CO 14.00 μmol g^{-1} h^{-1} for CH_4	Reaction stability > 64h	[78]
31	Cs_2SnI_6 NCs/SnS_2 nanosheet	Solid-vapor (H_2O+CH_3OH)	Xe-lamp 150 mW cm^{-2} 400nm filter	Cs_2SnI_6 (1.0)/SnS_2: 6.09 μmol g^{-1} for CH_4 (10h)	Reaction stability > 9h	[85]
32	$A_3Bi_2I_9$ nanocrystals	Solid-vapor	UV lamp (32W, 305 nm, 80.38 μW cm^{-2}	a. $Cs_3Bi_2I_9$ nanocrystals: 77.6 μmol g^{-1} for CO (10h) 14.9±0.8 μmol g^{-1} for CH_4 (10h) b. $Rb_3Bi_2I_9$ nanocrystals: 18.2 μmol g^{-1} for CO (10h) 17.0±1.6 μmol g^{-1} 1 for CH_4 (10h) c. $MA_3Bi_2I_9$ nanocrystals: 7.2 μmol g^{-1} for CO (10h) 9.8±0.6 μmol g^{-1} for CH_4 (10h)	Moisture stability: ⩾ 7days (RH=70%) Illumination stability ⩾12h (after 7 days of aging)	[86]
33	$Cs_3Bi_2X_9$ nanocrystals	Solid-vapor	300W Xe lamp, AM 1.5G filter	a. $Cs_3Bi_2Br_9$ nanorystals: 134.76 μmol g^{-1} for CO (5h) 300 μmol g^{-1} for CO (20h) b. $Cs_3Bi_2Cl_9$ nanorystals: 83.06 μmol g^{-1} for CO (5h) c. $Cs_3Bi_2I_9$ nanorystals: 5.78 μmol g^{-1} for CO (5h)	Reaction stability > 20h	[87]
34	$Cs_3Bi_2I_9$/Bi_2WO_6	Solid-vapor	300 W Xe lamp, 400 nm filter 100 mW cm^{-2}	a. $Cs_3Bi_2I_9$/Bi_2WO_6: 66 μmol g^{-1} for CO (9h) b. Pristine $Cs_3Bi_2I_9$: 15.2 μmol g^{-1} for CO (9h)	Reaction stability > 18h	[88]
35	$Cs_3Sb_2Br_9$ nanocrystal	Solid-liquid (ODE/H_2O)	300W Xe- lamp AM1.5G filter 100 mW cm^{-2}	a. $Cs_3Sb_2I_9$ nanocrystal: 510 μmol g^{-1} for CO (4h) b. Pristine $CsPbBr_3$ nanocrystal: 50 μmol g^{-1} for CO (4h)	Reaction stability > 9h	[89]
36	$Cs_3Sb_2I_9$	Solid-vapor	Xenon lamp 200 mW cm^{-2}	95.7 μmol g^{-1} h^{-1} for CO	--	[90]
37	Cs_2AgBiX_6 nanocrystals	Solid-vapor	300W Xe-lamp 420 nm filter	a. Cs_2AgBiI_6 nanocrystal: 18.9 μmol g^{-1} for CO (6h) b. $Cs_2AgBiCl_6$ nanocrystal: 13.62 μmol g^{-1} for CO (6h) c. $Cs_2AgBi(Br_{0.5}I_{0.5})_6$ nanocrystals: 11.88 μmol g^{-1} for CO (6h)	--	[91]
38	Cs_2AgBiX_6 (X=Cl, Br, I) double perovskite nanoplatelets	Solid-liquid (pure EA)	405 nm laser diode with a maximum power of 40 mM (from Thorlabs)	a. $Cs_2AgBiBr_6$ NPLs: Total photocatalytic electron consumption= 255.4 μmol g^{-1} b. $Cs_2AgBiBr_6$ NCs: Total photocatalytic electron consumption= 30.8 μmol g^{-1}	Reaction stability > 9h	[92]
39	$Cs_2AgInCl_6$@Ag-2	Solid-liquid (ethyl alcohol)	300W Xe-lamp	26.4 μmol g^{-1} for CO (4h) 28.9 μmol g^{-1} for CH_4 (4h)	Reaction stability > 9h	[44]
40	Cs_2CuBr_4 QDs	Solid-vapor	300 W Xe lamp (1.5G filter)	a. Cs_2CuBr_4 QDs: 74.81 μ mol g^{-1} for CH_4 (5h) 148.98 μ mol g^{-1} for CO (5h) b. Pristine $CsPbBr_3$ QDs:	Reaction stability > 20 h	[93]

				18.24 μ mol g^{-1} for CO (5h)		
41	$CsCuCl_3$ and $CsCuCl_2Br$ MCs	Solid-liquid (EA/IPA)	AM1.5 G 100 mW cm^{-2}	a. $CsCuCl_3$ MCs: 2.79 μ mol g^{-1} for CO (3h) 11.55 μ mol g−1 for CH_4 (3h) 103.9 μ mol g^{-1} for CO+CH_4 (20h) b. $CsCuCl_2Br$ MCs: 5.61 μ mol g^{-1} for CO (3h) 15.36 μ mol g^{-1} for CH_4 (3h) 153.4 μ mol g^{-1} for CO+CH_4 (20h)	Reaction stability >20h	[94]
42	Cs_2XCl_6 (X=Hf, Zr, Te) MCs	Solid-vapor	300 W Xe lamp	a. Cs_2TeCl_6 MCs: 284.4 μ mol g^{-1} for CO (3h) 48.96 μ mol g^{-1} for CH_4 (3h) b. Cs_2HfCl_6 MCs: 204.3 μ mol g^{-1} for CO (3h) 48.66 μ mol g^{-1} for CH_4 (3h) c. Cs_2ZrCl_6 MCs: 219.2 μ mol g^{-1} for CO (3h) 48.36 μ mol g^{-1} for CH_4 (3h)	Heating at 100℃ or irradiating with 365 nm UV lamp for 120 h or storage in air for 90 days	[95]

Credit Author Statement

Huilong Liu: Investigation; Writing-Original draft preparation; Writing-Reviewing and Editing.
Shubhra Bansal: Supervision; Writing-Reviewing and Editing.

Declaration of Competing Interest

The authors declare that they have no known competing financial interests or personal relationships that could have appeared to influence the work reported in this paper.

Acknowledgments

Funding: This work was supported by the NSF CAREER award [2046944]

References

[1] W. Gao, S. Liang, R. Wang, Q. Jiang, Y. Zhang, Q. Zheng, B. Xie, C.Y. Toe, X. Zhu, J. Wang, L. Huang, Y. Gao, Z. Wang, C. Jo, Q. Wang, L. Wang, Y. Liu, B. Louis, J. Scott, A.C. Roger, R. Amal, H. He, S.E. Park, Industrial carbon dioxide capture and utilization: State of the art and future challenges, Chem. Soc. Rev. 49 (2020) 8584–8686. https://doi.org/10.1039/d0cs00025f.

[2] M. Mendez-Galvan, B. Alcantar-Vazquez, G. Diaz, I.A. Ibarra, H.A. Lara-Garcia, Metal halide perovskites as an emergent catalyst for CO_2 photoreduction: A minireview, React. Chem. Eng. 6 (2021) 828–838. https://doi.org/10.1039/d1re00039j.

[3] D. Kim, K.K. Sakimoto, D. Hong, P. Yang, Artificial photosynthesis for sustainable fuel and chemical production, Angew. Chemie - Int. Ed. 54 (2015) 3259–3266. https://doi.org/10.1002/anie.201409116.

[4] E. Gong, S. Ali, C.B. Hiragond, H.S. Kim, N.S. Powar, D. Kim, H. Kim, S. Il In, Solar fuels: research and development strategies to accelerate photocatalytic CO_2 conversion into hydrocarbon fuels, Energy Environ. Sci. 15 (2021) 880–937. https://doi.org/10.1039/d1ee02714j.

[5] K. Honda, T. Inoue, A. Fujishima, S. Konishi, Photoelectrocatalytic reduction of carbon dioxide in aqueous suspensions of semiconductor . powders Highly efficient quantum conversion at chlorophyll a-lecithin mixed monolayer coated electrodes, Nature. 277 (1979) 637.

[6] A. Kumar, P.R. Thakur, G. Sharma, M. Naushad, A. Rana, G.T. Mola, F.J. Stadler, Carbon nitride, metal nitrides, phosphides, chalcogenides, perovskites and carbides nanophotocatalysts for environmental applications, Environ. Chem. Lett. 17 (2019) 655–682. https://doi.org/10.1007/s10311-018-0814-8.

[7] S. Das, W.M.A. Wan Daud, A review on advances in photocatalysts towards CO_2 conversion, RSC Adv. 4 (2014) 20856–20893. https://doi.org/10.1039/c4ra01769b.

[8] A. Razzaq, A. Sinhamahapatra, T.H. Kang, C.A. Grimes, J.S. Yu, S. Il In, Efficient solar light photoreduction of CO_2 to hydrocarbon fuels via magnesiothermally reduced TiO_2 photocatalyst, Appl. Catal. B Environ. 215 (2017) 28–35. https://doi.org/10.1016/j.apcatb.2017.05.028.

[9] A. Akhundi, A. Habibi-Yangjeh, M. Abitorabi, S. Rahim Pouran, Review on photocatalytic conversion of carbon dioxide to value-added compounds and renewable fuels by graphitic carbon nitride-based photocatalysts, Catal. Rev. Sci. Eng. 61 (2019) 595–628. https://doi.org/10.1080/01614940.2019.1654224.

[10] H. Wu, X. Li, C. Tung, L. Wu, Semiconductor Quantum Dots: An Emerging Candidate for CO_2 Photoreduction, Adv. Mater. 31 (2019) 1900709. https://doi.org/10.1002/adma.201900709.
[11] X. Jiao, K. Zheng, L. Liang, X. Li, Y. Sun, Y. Xie, Fundamentals and challenges of ultrathin 2D photocatalysts in boosting CO_2 photoreduction, Chem. Soc. Rev. 49 (2020) 6592–6604. https://doi.org/10.1039/d0cs00332h.
[12] T.P. Nguyen, D.L.T. Nguyen, V.-H. Nguyen, T.-H. Le, D.-V.N. Vo, Q.T. Trinh, S.-R. Bae, S.Y. Chae, S.Y. Kim, Q. Van Le, Recent Advances in TiO_2-Based Photocatalysts for Reduction of CO_2 to Fuels, Nanomaterials. 10 (2020) 337. https://doi.org/10.3390/nano10020337.
[13] C.B. Hiragond, J. Lee, H. Kim, J.W. Jung, C.H. Cho, S. Il In, A novel N-doped graphene oxide enfolded reduced titania for highly stable and selective gas-phase photocatalytic CO_2 reduction into CH_4: An in-depth study on the interfacial charge transfer mechanism, Chem. Eng. J. 416 (2021) 1–12. https://doi.org/10.1016/j.cej.2020.127978.
[14] J.W. Maina, C. Pozo-Gonzalo, L. Kong, J. Schütz, M. Hill, L.F. Dumée, Metal organic framework based catalysts for CO_2 conversion, Mater. Horizons. 4 (2017) 345–361. https://doi.org/10.1039/c6mh00484a.
[15] S. Xie, Q. Zhang, G. Liu, Y. Wang, Photocatalytic and photoelectrocatalytic reduction of CO_2 using heterogeneous catalysts with controlled nanostructures, Chem. Commun. 52 (2016) 35–59. https://doi.org/10.1039/c5cc07613g.
[16] C.B. Hiragond, N.S. Powar, S.-I. In, Recent Developments in Lead and Lead-Free Halide Perovskite Nanostructures towards Photocatalytic CO_2 Reduction, Nanomaterials. 10 (2020) 2569. https://doi.org/10.3390/nano10122569.
[17] M. Singh, I. Sinha, Halide perovskite-based photocatalysis systems for solar-driven fuel generation, Sol. Energy. 208 (2020) 296–311. https://doi.org/10.1016/j.solener.2020.08.007.
[18] B. Saparov, D.B. Mitzi, Organic-Inorganic Perovskites: Structural Versatility for Functional Materials Design, Chem. Rev. 116 (2016) 4558–4596. https://doi.org/10.1021/acs.chemrev.5b00715.
[19] Q.A. Akkerman, G. Rainò, M. V. Kovalenko, L. Manna, Genesis, challenges and opportunities for colloidal lead halide perovskite nanocrystals, Nat. Mater. 17 (2018) 394–405. https://doi.org/10.1038/s41563-018-0018-4.
[20] X. Li, F. Cao, D. Yu, J. Chen, Z. Sun, Y. Shen, Y. Zhu, L. Wang, Y. Wei, Y. Wu, H. Zeng, All Inorganic Halide Perovskites Nanosystem: Synthesis, Structural Features, Optical Properties and Optoelectronic Applications, Small. 13 (2017) 1–24. https://doi.org/10.1002/smll.201603996.
[21] A. Dey, J. Ye, A. De, E. Debroye, S.K. Ha, E. Bladt, A.S. Kshirsagar, Z. Wang, J. Yin, Y. Wang, L.N. Quan, F. Yan, M. Gao, X. Li, J. Shamsi, T. Debnath, M. Cao, M.A. Scheel, S. Kumar, J.A. Steele, M. Gerhard, L. Chouhan, K. Xu, X.G. Wu, Y. Li, Y. Zhang, A. Dutta, C. Han, I. Vincon, A.L. Rogach, A. Nag, A. Samanta, B.A. Korgel, C.-J.J. Shih, D.R. Gamelin, D.H. Son, H. Zeng, H. Zhong, H. Sun, H.V. Demir, I.G. Scheblykin, I. Mora-Seró, J.K. Stolarczyk, J.Z. Zhang, J. Feldmann, J. Hofkens, J.M. Luther, J. Pérez-Prieto, L. Li, L. Manna, M.I. Bodnarchuk, M. V. Kovalenko, M.B.J.J. Roeffaers, N. Pradhan, O.F. Mohammed, O.M. Bakr, P. Yang, P. Müller-Buschbaum, P. V. Kamat, Q. Bao, Q. Zhang, R. Krahne, R.E. Galian, S.D. Stranks, S. Bals, V. Biju, W.A. Tisdale, Y. Yan, R.L.Z.Z. Hoye, L. Polavarapu, State of the Art and Prospects for Halide Perovskite Nanocrystals, ACS Nano. 15 (2021) 10775–10981. https://doi.org/10.1021/acsnano.0c08903.
[22] Y. Wang, G. Ding, J.Y. Mao, Y. Zhou, S.T. Han, Recent advances in synthesis and application of perovskite quantum dot based composites for photonics, electronics and sensors, Sci. Technol. Adv. Mater. 21 (2020) 278–302. https://doi.org/10.1080/14686996.2020.1752115.
[23] M. V. Kovalenko, L. Protesescu, M.I. Bodnarchuk, Properties and potential optoelectronic applications of lead halide perovskite nanocrystals, Science (80). 358 (2017) 745–750. https://doi.org/10.1126/science.aam7093.
[24] H. Huang, B. Pradhan, J. Hofkens, M.B.J. Roeffaers, J.A. Steele, Solar-Driven Metal Halide Perovskite Photocatalysis: Design, Stability, and Performance, ACS Energy Lett. 5 (2020) 1107–1123. https://doi.org/10.1021/acsenergylett.0c00058.
[25] C. Han, X. Zhu, J.S. Martin, Y. Lin, S. Spears, Y. Yan, Recent Progress in Engineering Metal Halide Perovskites for Efficient Visible-Light-Driven Photocatalysis, ChemSusChem. 13 (2020) 4005–4025. https://doi.org/10.1002/cssc.202000953.
[26] K.A. Huynh, D.L.T. Nguyen, V.H. Nguyen, D.V.N. Vo, Q.T. Trinh, T.P. Nguyen, S.Y. Kim, Q. Van Le, Halide perovskite photocatalysis: progress and perspectives, J. Chem. Technol. Biotechnol. 95 (2020) 2579–2596. https://doi.org/10.1002/jctb.6342.
[27] S. Pan, J. Li, Z. Wen, R. Lu, Q. Zhang, H. Jin, L. Zhang, Y. Chen, S. Wang, Halide Perovskite Materials for Photo(Electro)Chemical Applications: Dimensionality, Heterojunction, and Performance, Adv. Energy Mater. 12 (2022) 1–38. https://doi.org/10.1002/aenm.202004002.
[28] J. Wang, Y. Shi, Y. Wang, Z. Li, Rational Design of Metal Halide Perovskite Nanocrystals for Photocatalytic CO_2 Reduction: Recent Advances, Challenges, and Prospects , ACS Energy Lett. 7 (2022) 2043–2059. https://doi.org/10.1021/acsenergylett.2c00752.
[29] Z. Zhang, Y. Jiang, M. Shu, L. Li, Z. Dong, J. Xu, Artificial Photosynthesis over Metal Halide Perovskites: Achievements, Challenges, and Prospects, J. Phys. Chem. Lett. 12 (2021) 5864–5870. https://doi.org/10.1021/acs.jpclett.1c01527.
[30] J. Hou, S. Cao, Y. Wu, Z. Gao, F. Liang, Y. Sun, Z. Lin, L. Sun, Inorganic Colloidal Perovskite Quantum Dots for Robust Solar CO_2 Reduction, Chem. – A Eur. J. 23 (2017) 9481–9485. https://doi.org/10.1002/chem.201702237.
[31] G. Zhang, G. Liu, L. Wang, J.T.S. Irvine, Inorganic perovskite photocatalysts for solar enerzgy utilization, Chem. Soc. Rev. 45 (2016) 5951–5984. https://doi.org/10.1039/c5cs00769k.
[32] S. Shyamal, N. Pradhan, Halide Perovskite Nanocrystal Photocatalysts for CO_2 Reduction: Successes and Challenges, J. Phys. Chem. Lett. 11 (2020) 6921–6934. https://doi.org/10.1021/acs.jpclett.0c00191.
[33] L. Protesescu, S. Yakunin, M.I. Bodnarchuk, F. Krieg, R. Caputo, C.H. Hendon, R.X. Yang, A. Walsh, M. V. Kovalenko, Nanocrystals of Cesium Lead Halide Perovskites ($CsPbX_3$, X = Cl, Br, and I): Novel Optoelectronic Materials Showing Bright

Emission with Wide Color Gamut, Nano Lett. 15 (2015) 3692–3696. https://doi.org/10.1021/nl5048779.
[34] F. Brivio, K.T. Butler, A. Walsh, M. Van Schilfgaarde, Relativistic quasiparticle self-consistent electronic structure of hybrid halide perovskite photovoltaic absorbers, Phys. Rev. B - Condens. Matter Mater. Phys. 89 (2014) 1–6. https://doi.org/10.1103/PhysRevB.89.155204.
[35] T. Umebayashi, K. Asai, T. Umebayashi, K. Asai, T. Kondo, T. Kondo, A. Nakao, Electronic structures of lead iodide based low-dimensional crystals, Phys. Rev. B - Condens. Matter Mater. Phys. 67 (2003) 2–7. https://doi.org/10.1103/PhysRevB.67.155405.
[36] L.Y. Wu, M.R. Zhang, Y.X. Feng, W. Zhang, M. Zhang, T.B. Lu, Two-Dimensional Metal Halide Perovskite Nanosheets for Efficient Photocatalytic CO_2 Reduction, Sol. RRL. 5 (2021) 1–9. https://doi.org/10.1002/solr.202100263.
[37] S. Shyamal, S.K. Dutta, T. Das, S. Sen, S. Chakraborty, N. Pradhan, Facets and Defects in Perovskite Nanocrystals for Photocatalytic CO_2 Reduction, J. Phys. Chem. Lett. 11 (2020) 3608–3614. https://doi.org/10.1021/acs.jpclett.0c01088.
[38] X. Li, Y. Wu, S. Zhang, B. Cai, Y. Gu, J. Song, H. Zeng, $CsPbX_3$ Quantum Dots for Lighting and Displays: Roomerature Synthesis, Photoluminescence Superiorities, Underlying Origins and White Light-Emitting Diodes, Adv. Funct. Mater. 26 (2016) 2435–2445. https://doi.org/10.1002/adfm.201600109.
[39] D. Yang, X. Li, W. Zhou, S. Zhang, C. Meng, Y. Wu, Y. Wang, H. Zeng, CsPbBr3 Quantum Dots 2.0: Benzenesulfonic Acid Equivalent Ligand Awakens Complete Purification, Adv. Mater. 31 (2019) 1–8. https://doi.org/10.1002/adma.201900767.
[40] J. Zhu, Y. Zhu, J. Huang, L. Hou, J. Shen, C. Li, Synthesis of monodisperse water-stable surface Pb-rich $CsPbCl_3$ nanocrystals for efficient photocatalytic CO2reduction, Nanoscale. 12 (2020) 11842–11846. https://doi.org/10.1039/d0nr02917c.
[41] V.K. Ravi, P.K. Santra, N. Joshi, J. Chugh, S.K. Singh, H. Rensmo, P. Ghosh, A. Nag, Origin of the Substitution Mechanism for the Binding of Organic Ligands on the Surface of $CsPbBr_3$ Perovskite Nanocubes, J. Phys. Chem. Lett. 8 (2017) 4988–4994. https://doi.org/10.1021/acs.jpclett.7b02192.
[42] D. Yang, X. Li, Y. Wu, C. Wei, Z. Qin, C. Zhang, Z. Sun, Y. Li, Y. Wang, H. Zeng, Surface Halogen Compensation for Robust Performance Enhancements of $CsPbX_3$ Perovskite Quantum Dots, Adv. Opt. Mater. 7 (2019) 1–10. https://doi.org/10.1002/adom.201900276.
[43] L. Zhou, Y.F. Xu, B.X. Chen, D. Bin Kuang, C.Y. Su, Synthesis and Photocatalytic Application of Stable Lead-Free $Cs_2AgBiBr_6$ Perovskite Nanocrystals, Small. 14 (2018) 1–7. https://doi.org/10.1002/smll.201703762.
[44] T. Chen, M. Zhou, W. Chen, Y. Zhang, S. Ou, Y. Liu, $Cs_2AgInCl_6$ double perovskite quantum dots decorated with Ag nanoparticles for photocatalytic CO_2 reduction, Sustain. Energy Fuels. 5 (2021) 3598–3605. https://doi.org/10.1039/d1se00754h.
[45] Z. Chen, Y. Hu, J. Wang, Q. Shen, Y. Zhang, C. Ding, Y. Bai, G. Jiang, Z. Li, N. Gaponik, Boosting Photocatalytic CO_2 Reduction on $CsPbBr_3$ Perovskite Nanocrystals by Immobilizing Metal Complexes, Chem. Mater. 32 (2020) 1517–1525. https://doi.org/10.1021/acs.chemmater.9b04582.
[46] R. Cheng, C.C. Chung, S. Wang, B. Cao, M. Zhang, C. Chen, Z. Wang, M. Chen, S. Shen, S.P. Feng, Three-dimensional self-attaching perovskite quantum dots/polymer platform for efficient solar-driven CO_2 reduction, Mater. Today Phys. 17 (2021) 100358. https://doi.org/10.1016/j.mtphys.2021.100358.
[47] C. Tang, C. Chen, W. Xu, L. Xu, Design of doped cesium lead halide perovskite as a photo-catalytic CO_2 reduction catalyst, J. Mater. Chem. A. 7 (2019) 6911–6919. https://doi.org/10.1039/c9ta00550a.
[48] G.X. Dong, W. Zhang, Y.F. Mu, K. Su, M. Zhang, T.B. Lu, A halide perovskite as a catalyst to simultaneously achieve efficient photocatalytic CO_2 reduction and methanol oxidation, Chem. Commun. 56 (2020) 4664–4667. https://doi.org/10.1039/d0cc01176b.
[49] S. Shyamal, S.K. Dutta, N. Pradhan, Doping Iron in $CsPbBr_3$ Perovskite Nanocrystals for Efficient and Product Selective CO_2 Reduction, J. Phys. Chem. Lett. 10 (2019) 7965–7969. https://doi.org/10.1021/acs.jpclett.9b03176.
[50] Y. Liu, S. Guo, S. You, C. Sun, Mn-doped $CsPb(Br/Cl)_3$ mixed-halide perovskites for CO_2 photoreduction, Nanotechnology. 3 (2020) 0–5.
[51] G. Huang, C. Wang, S. Xu, S. Zong, J. Lu, Z. Wang, C. Lu, Y. Cui, Postsynthetic Doping of $MnCl_2$ Molecules into Preformed $CsPbBr_3$ Perovskite Nanocrystals via a Halide Exchange-Driven Cation Exchange, Adv. Mater. 29 (2017) 10–14. https://doi.org/10.1002/adma.201700095.
[52] G. Nedelcu, L. Protesescu, S. Yakunin, M.I. Bodnarchuk, M.J. Grotevent, M. V. Kovalenko, Fast Anion-Exchange in Highly Luminescent Nanocrystals of Cesium Lead Halide Perovskites ($CsPbX_3$, X = Cl, Br, I), Nano Lett. 15 (2015) 5635–5640. https://doi.org/10.1021/acs.nanolett.5b02404.
[53] J. Cheng, Y. Mu, L. Wu, Z. Liu, K. Su, G. Dong, M. Zhang, T. Lu, Acetate-assistant efficient cation-exchange of halide perovskite nanocrystals to boost the photocatalytic CO_2 reduction, Nano Res. (2021). https://doi.org/10.1007/s12274-021-3775-3.
[54] Q. Xu, L. Zhang, B. Cheng, J. Fan, J. Yu, S-Scheme Heterojunction Photocatalyst, Chem. 6 (2020) 1543–1559. https://doi.org/10.1016/j.chempr.2020.06.010.
[55] Y.F. Xu, M.Z. Yang, B.X. Chen, X.D. Wang, H.Y. Chen, D. Bin Kuang, C.Y. Su, A $CsPbBr_3$ Perovskite Quantum Dot/Graphene Oxide Composite for Photocatalytic CO_2 Reduction, J. Am. Chem. Soc. 139 (2017) 5660–5663. https://doi.org/10.1021/jacs.7b00489.
[56] Y.F. Xu, M.Z. Yang, H.Y. Chen, J.F. Liao, X.D. Wang, D. Bin Kuang, Enhanced Solar-Driven Gaseous CO_2 Conversion by $CsPbBr_3$ Nanocrystal/Pd Nanosheet Schottky-Junction Photocatalyst, ACS Appl. Energy Mater. 1 (2018) 5083–5089. https://doi.org/10.1021/acsaem.8b01133.
[57] Y. Jiang, J.F. Liao, Y.F. Xu, H.Y. Chen, X.D. Wang, D. Bin Kuang, Hierarchical $CsPbBr_3$ nanocrystal-decorated ZnO nanowire/macroporous graphene hybrids for enhancing charge separation and photocatalytic CO_2 reduction, J. Mater. Chem. A. 7 (2019) 13762–13769. https://doi.org/10.1039/c9ta03478a.

[58] A. Pan, X. Ma, S. Huang, Y. Wu, M. Jia, Y. Shi, Y. Liu, P. Wangyang, L. He, Y. Liu, $CsPbBr_3$ Perovskite Nanocrystal Grown on MXene Nanosheets for Enhanced Photoelectric Detection and Photocatalytic CO_2 Reduction, J. Phys. Chem. Lett. 10 (2019) 6590–6597. https://doi.org/10.1021/acs.jpclett.9b02605.

[59] Z.C. Kong, H.H. Zhang, J.F. Liao, Y.J. Dong, Y. Jiang, H.Y. Chen, D. Bin Kuang, Immobilizing $Re(CO)_3Br(dcbpy)$ Complex on $CsPbBr_3$ Nanocrystal for Boosted Charge Separation and Photocatalytic CO_2 Reduction, Sol. RRL. 4 (2020) 2–8. https://doi.org/10.1002/solr.201900365.

[60] M. Ou, W. Tu, S. Yin, W. Xing, S. Wu, H. Wang, S. Wan, Q. Zhong, R. Xu, Amino-Assisted Anchoring of $CsPbBr_3$ Perovskite Quantum Dots on Porous g-C_3N_4 for Enhanced Photocatalytic CO_2 Reduction, Angew. Chemie - Int. Ed. 57 (2018) 13570–13574. https://doi.org/10.1002/anie.201808930.

[61] L. Jiao, Y. Wang, H.L. Jiang, Q. Xu, Metal–Organic Frameworks as Platforms for Catalytic Applications, Adv. Mater. 30 (2018) 1–23. https://doi.org/10.1002/adma.201703663.

[62] Z.-C. Kong, J.-F. Liao, Y.-J. Dong, Y.-F. Xu, H.-Y. Chen, D.-B. Kuang, C.-Y. Su, Core@Shell $CsPbBr_3$ @Zeolitic Imidazolate Framework Nanocomposite for Efficient Photocatalytic CO_2 Reduction, ACS Energy Lett. 3 (2018) 2656–2662. https://doi.org/10.1021/acsenergylett.8b01658.

[63] S. Wan, M. Ou, Q. Zhong, X. Wang, Perovskite-type $CsPbBr_3$ quantum dots/UiO-66(NH_2) nanojunction as efficient visible-light-driven photocatalyst for CO_2 reduction, Chem. Eng. J. 358 (2019) 1287–1295. https://doi.org/10.1016/j.cej.2018.10.120.

[64] L.Y. Wu, Y.F. Mu, X.X. Guo, W. Zhang, Z.M. Zhang, M. Zhang, T.B. Lu, Encapsulating Perovskite Quantum Dots in Iron-Based Metal–Organic Frameworks (MOFs) for Efficient Photocatalytic CO_2 Reduction, Angew. Chemie - Int. Ed. 58 (2019) 9491–9495. https://doi.org/10.1002/anie.201904537.

[65] X. Wang, J. He, L. Mao, X. Cai, C. Sun, M. Zhu, $CsPbBr_3$ perovskite nanocrystals anchoring on monolayer MoS_2 nanosheets for efficient photocatalytic CO_2 reduction, Chem. Eng. J. 416 (2021) 2–10. https://doi.org/10.1016/j.cej.2020.128077.

[66] N. Zhang, J.J. Li, Y. Li, H. Wang, J.Y. Zhang, Y. Liu, Y.Z. Fang, Z. Liu, M. Zhou, Visible-light driven boosting electron-hole separation in $CsPbBr_3$ QDs@2D Cu-TCPP heterojunction and the efficient photoreduction of CO_2, J. Colloid Interface Sci. 608 (2021) 3192–3203. https://doi.org/10.1016/j.jcis.2021.11.045.

[67] Y. Jiang, J.F. Liao, H.Y. Chen, H.H. Zhang, J.Y. Li, X.D. Wang, D. Bin Kuang, All-Solid-State Z-Scheme α-Fe_2O_3/Amine-RGO/$CsPbBr_3$ Hybrids for Visible-Light-Driven Photocatalytic CO_2 Reduction, Chem. 6 (2020) 766–780. https://doi.org/10.1016/j.chempr.2020.01.005.

[68] Y.F. Mu, W. Zhang, G.X. Dong, K. Su, M. Zhang, T.B. Lu, Ultrathin and Small-Size Graphene Oxide as an Electron Mediator for Perovskite-Based Z-Scheme System to Significantly Enhance Photocatalytic CO_2 Reduction, Small. 16 (2020) 1–8. https://doi.org/10.1002/smll.202002140.

[69] H. Huang, J. Zhao, Y. Du, C. Zhou, M. Zhang, Z. Wang, Y. Weng, J. Long, J. Hofkens, J.A. Steele, M.B.J. Roeffaers, Direct Z-Scheme Heterojunction of Semicoherent $FAPbBr_3/Bi_2WO_6$ Interface for Photoredox Reaction with Large Driving Force, ACS Nano. 14 (2020) 16689–16697. https://doi.org/10.1021/acsnano.0c03146.

[70] J. Wang, J. Wang, N. Li, X. Du, J. Ma, C. He, Z. Li, Direct Z-Scheme 0D/2D Heterojunction of $CsPbBr_3$ Quantum Dots/Bi_2WO_6 Nanosheets for Efficient Photocatalytic CO_2 Reduction., ACS Appl. Mater. Interfaces. 12 (2020) 31477–31485. https://doi.org/10.1021/acsami.0c08152.

[71] Z. Dong, Z. Zhang, Y. Jiang, Y. Chu, J. Xu, Embedding $CsPbBr_3$ perovskite quantum dots into mesoporous TiO_2 beads as an S-scheme heterojunction for CO_2 photoreduction, Chem. Eng. J. (2021) 133762. https://doi.org/10.1016/j.cej.2021.133762.

[72] Y. Wei, Z. Cheng, J. Lin, An overview on enhancing the stability of lead halide perovskite quantum dots and their applications in phosphor-converted LEDs, Chem. Soc. Rev. 48 (2019) 310–350. https://doi.org/10.1039/c8cs00740c.

[73] Q. Chen, Y. Ma, L. Wang, X. Lan, J. Shi, Multifunctional Melamine Foam Assisted Lead Halide Perovskites for Highly Efficient and Long-Term Photocatalytic CO_2 Reduction Under Pure Water, Sol. RRL. 5 (2021) 1–10. https://doi.org/10.1002/solr.202000755.

[74] Y.X. Chen, Y.F. Xu, X.D. Wang, H.Y. Chen, D. Bin Kuang, Solvent selection and Pt decoration towards enhanced photocatalytic CO_2 reduction over $CsPbBr_3$ perovskite single crystals, Sustain. Energy Fuels. 4 (2020) 2249–2255. https://doi.org/10.1039/c9se01218d.

[75] D. Wu, X. Zhao, Y. Huang, J. Lai, J. Yang, C. Tian, P. He, Q. Huang, X. Tang, Synthesis and CO_2 Photoreduction of Lead-Free Cesium Bismuth Halide Perovskite Nanocrystals, J. Phys. Chem. C. 125 (2021) 18328–18333. https://doi.org/10.1021/acs.jpcc.1c05110.

[76] Y.F. Mu, W. Zhang, X.X. Guo, G.X. Dong, M. Zhang, T.B. Lu, Water-Tolerant Lead Halide Perovskite Nanocrystals as Efficient Photocatalysts for Visible-Light-Driven CO_2 Reduction in Pure Water, ChemSusChem. 12 (2019) 4769–4774. https://doi.org/10.1002/cssc.201902192.

[77] Q. Chen, X. Lan, Y. Ma, P. Lu, Z. Yuan, J. Shi, Boosting $CsPbBr_3$-Driven Superior and Long-Term Photocatalytic CO_2 Reduction under Pure Water Medium: Synergy Effects of Multifunctional Melamine Foam and Graphitic Carbon Nitride (g-C_3N_4), Sol. RRL. 5 (2021) 1–12. https://doi.org/10.1002/solr.202100186..

[78] Y. Zhang, L. Shi, H. Yuan, X. Sun, X. Li, L. Duan, Q. Li, Z. Huang, X. Ban, D.E. Zhang, Construction of melamine foam–supported WO_3/$CsPbBr_3$ S–scheme heterojunction with rich oxygen vacancies for efficient and long–period CO_2 photoreduction in liquid–phase H_2O environment, Chem. Eng. J. 430 (2022) 132820. https://doi.org/10.1016/j.cej.2021.132820.

[79] L. Chu, W. Ahmad, W. Liu, J. Yang, R. Zhang, Y. Sun, J. Yang, X. Li, Lead-Free Halide Double Perovskite Materials: A New Superstar Toward Green and Stable Optoelectronic Applications, Nano-Micro Lett. 11 (2019) 1–18. https://doi.org/10.1007/s40820-019-0244-6.

[80] J. Li, H.L. Cao, W. Bin Jiao, Q. Wang, M. Wei, I. Cantone, J. Lü, A. Abate, Biological impact of lead from halide perovskites reveals the risk of introducing a safe threshold, Nat. Commun. 11 (2020) 1–5. https://doi.org/10.1038/s41467-019-13910-y.
[81] Q. Fan, G. V. Biesold-McGee, J. Ma, Q. Xu, S. Pan, J. Peng, Z. Lin, Lead-Free Halide Perovskite Nanocrystals: Crystal Structures, Synthesis, Stabilities, and Optical Properties, Angew. Chemie - Int. Ed. 59 (2020) 1030–1046. https://doi.org/10.1002/anie.201904862.
[82] S. Ghosh, B. Pradhan, Lead-Free Metal Halide Perovskite Nanocrystals: Challenges, Applications, and Future Aspects, ChemNanoMat. 5 (2019) 300–312. https://doi.org/10.1002/cnma.201800645.
[83] T.C. Jellicoe, J.M. Richter, H.F.J. Glass, M. Tabachnyk, R. Brady, S.E. Dutton, A. Rao, R.H. Friend, D. Credgington, N.C. Greenham, M.L. Böhm, Synthesis and Optical Properties of Lead-Free Cesium Tin Halide Perovskite Nanocrystals, J. Am. Chem. Soc. 138 (2016) 2941–2944. https://doi.org/10.1021/jacs.5b13470.
[84] A. Wang, X. Yan, M. Zhang, S. Sun, M. Yang, W. Shen, X. Pan, P. Wang, Z. Deng, Controlled synthesis of lead-free and stable perovskite derivative Cs_2SnI_6 nanocrystals via a facile hot-injection process, Chem. Mater. 28 (2016) 8132–8140. https://doi.org/10.1021/acs.chemmater.6b01329.
[85] X.D. Wang, Y.H. Huang, J.F. Liao, Y. Jiang, L. Zhou, X.Y. Zhang, H.Y. Chen, D. Bin Kuang, In Situ Construction of a Cs_2SnI_6 Perovskite Nanocrystal/SnS_2 Nanosheet Heterojunction with Boosted Interfacial Charge Transfer, J. Am. Chem. Soc. 141 (2019) 13434–13441. https://doi.org/10.1021/jacs.9b04482.
[86] S.S. Bhosale, A.K. Kharade, E. Jokar, A. Fathi, S.M. Chang, E.W.G. Diau, Mechanism of Photocatalytic CO_2 Reduction by Bismuth-Based Perovskite Nanocrystals at the Gas-Solid Interface, J. Am. Chem. Soc. 141 (2019) 20434–20442. https://doi.org/10.1021/jacs.9b11089.
[87] F. Dong, J. Sheng, Y. He, J. Li, C. Yuan, H. Huang, S. Wang, Y. Sun, Z. Wang, Identification of halogen-associated active sites on bismuth-based perovskite quantum dots for efficient and selective CO_2-to-CO photoreduction, ACS Nano. 14 (2020) 13103–13114. https://doi.org/10.1021/acsnano.0c04659.
[88] Z.L. Liu, R.R. Liu, Y.F. Mu, Y.X. Feng, G.X. Dong, M. Zhang, T.B. Lu, In Situ Construction of Lead-Free Perovskite Direct Z-Scheme Heterojunction $Cs_3Bi_2I_9/Bi_2WO_6$ for Efficient Photocatalysis of CO_2 Reduction, Sol. RRL. 5 (2021) 1–9. https://doi.org/10.1002/solr.202000691.
[89] C. Lu, D.S. Itanze, A.G. Aragon, X. Ma, H. Li, K.B. Ucer, C. Hewitt, D.L. Carroll, R.T. Williams, Y. Qiu, S.M. Geyer, Synthesis of lead-free $Cs_3Sb_2Br_9$ perovskite alternative nanocrystals with enhanced photocatalytic CO_2 reduction activity, Nanoscale. 12 (2020) 2987–2991. https://doi.org/10.1039/c9nr07722g.
[90] Y. Wang, Q. Zhou, Y. Zhu, D. Xu, High efficiency reduction of CO_2 to CO and CH_4 via photothermal synergistic catalysis of lead-free perovskite $Cs_3Sb_2I_9$, Appl. Catal. B Environ. 294 (2021) 120236. https://doi.org/10.1016/j.apcatb.2021.120236.
[91] D. Wu, X. Zhao, Y. Huang, J. Lai, H. Li, J. Yang, C. Tian, P. He, Q. Huang, X. Tang, Lead-free perovskite Cs_2AgBiX_6 nanocrystals with a band gap funnel structure for photocatalytic CO_2 reduction under visible light, Chem. Mater. 33 (2021) 4971–4976. https://doi.org/10.1021/acs.chemmater.1c00753.
[92] Z. Liu, H. Yang, J. Wang, Y. Yuan, K. Hills-Kimball, T. Cai, P. Wang, A. Tang, O. Chen, Synthesis of lead-free Cs_2AgBiX_6 (X = Cl, Br, I) double perovskite nanoplatelets and their application in CO_2 photocatalytic reduction, Nano Lett. 21 (2021) 1620–1627. https://doi.org/10.1021/acs.nanolett.0c04148.
[93] J. Sheng, Y. He, M. Huang, C. Yuan, S. Wang, F. Dong. Frustrated Lewis Pair Sites Boosting CO_2 Photoreduction on Cs_2CuBr_4 Perovskite Quantum Dots, ACS Catalysis. 12 (2022) 2915-2926. https://doi.org/10.1021/acscatal.2c00037.
[94] H. B. Zhao, J. F. liao, Y. Teng, H. Y. Chen, D. Bin. Kuang. Inorganic Copper-Based Halide Perovskite for Efficient Photocatalytic CO_2 Reduction, ACS Applied Materials and Interfaces. 14 (38) 43354-43361. https://doi.org/10.1021/acsami.2c12695.
[95] C. Tian, Q. Huang, D. Wu, J. Lai, F. Qi, N. Zhang, W. Zhang, X. Tang. Lead-free perovskite Cs_2XCl_6 (X=Hf, Zr, Te) microcrystals for photocatalytic CO_2 reduction, Materials Today Energy. 28 (2022) 101067. https://doi.org/10.1016/j.mtener.2022.101067.